UC San Diego
UC San Diego Previously Published Works

Title

Active Dipping Interface of the Southern San Andreas Fault Revealed by Space Geodetic and Seismic Imaging

Permalink

https://escholarship.org/uc/item/3kz8d184

Journal

Journal of Geophysical Research: Solid Earth, 128(11)

ISSN

2169-9313

Authors

Vavra, Ellis J

Qiu, Hongrui

Chi, Benxin

et al.

Publication Date

2023-11-01

DOI

10.1029/2023jb026811

Copyright Information

Peer reviewed

Active Dipping Interface of the Southern San Andreas Fault Revealed by Space Geodetic and Seismic Imaging

Ellis J. Vavra[1], Hongrui Qiu[2], Benxin Chi[3], Pieter-Ewald Share[4], Amir Allam[5], Matthias Morzfeld[1], Frank Vernon[1], Yehuda Ben-Zion[6], and Yuri Fialko[1]

[1]Institute of Geophysics and Planetary Physics, Scripps Institution of Oceanography, University of California, San Diego, La Jolla, CA, USA, [2]School of Geophysics and Geomatics, China University of Geosciences Wuhan, Wuhan, China, [3]State Key Laboratory of Geodesy and Earth's Dynamics, Innovation Academy for Precision Measurement Science and Technology, Chinese Academy of Sciences, Wuhan, China, [4]College of Earth, Ocean, and Atmospheric Sciences, Oregon State University, Corvallis, OR, USA, [5]Department of Geology and Geophysics, University of Utah, Salt Lake City, UT, USA, [6]Department of Earth Sciences and Southern California Earthquake Center, University of Southern California, Los Angeles, CA, USA

Abstract The Southern San Andreas Fault (SSAF) in California is one of the most thoroughly studied faults in the world, but its configuration at seismogenic depths remains enigmatic in the Coachella Valley. We use a combination of space geodetic and seismic observations to demonstrate that the relatively straight southernmost section of the SSAF, between Thousand Palms and Bombay Beach, is dipping to the northeast at 60–80° throughout the upper crust (<10 km), including the shallow aseismic layer. We constrain the fault attitude in the top 2–3 km using inversions of surface displacements associated with shallow creep, and seismic data from a dense nodal array crossing the fault trace near Thousand Palms. The data inversions show that the shallow dipping structure connects with clusters of seismicity at depth, indicating a continuous throughgoing fault surface. The dipping fault geometry has important implications for the long-term fault slip rate, the intensity of ground shaking during future large earthquakes, and the effective strength of the southern SAF.

Plain Language Summary The San Andreas Fault (SAF) is capable of large, destructive earthquakes and poses significant seismic hazard in California. In the Coachella Valley, the geometry of the SAF beneath the Earth's surface has been the subject of much debate. Here, we present new constraints on the fault's structure in the uppermost 2–3 km of the crust from several new sets of observations. We measure slow movement of the fault at the surface using satellite-based radar and perform simulations of what fault geometry is most likely to produce the observed motion. We also installed an array of sensors across the SAF to measure seismic waves that travel through or reflect off the fault. Analysis of both data sets indicates that the shallow portion of the SAF dips to the northeast in the Coachella Valley. Precise locations of small earthquakes at greater depths exhibit a similar trend—we thus suggest the fault dips throughout the Earth's crust. Better understanding the geometry of this section of the SAF has implications for earthquake hazards in Southern California, as well as the fault's geologic history.

1. Introduction

Large crustal earthquakes typically occur on faults with well-recognized surface expressions (Manighetti et al., 2007; Stirling et al., 1996). Fault geometries below the Earth's surface are typically not well-known, especially for faults that have remained quiescent in the instrumental era. Observations of recent large earthquakes have revealed often surprising rupture geometries that were not anticipated prior to the earthquake occurrence (e.g., Árnadóttir & Segall, 1994; Avouac et al., 2014; Fialko, 2004; Jin & Fialko, 2020; Tong et al., 2010). Improving our knowledge of the subsurface configuration of large active faults is thus important for evaluating possible rupture scenarios, predicting ground motion, and mitigating future seismic risks.

In this paper, we present new observational constraints on the subsurface geometry of the Coachella Valley section of the Southern San Andreas Fault (SSAF) in Southern California. The SSAF is a major plate boundary fault capable of great (magnitude 8 or larger) earthquakes (Figure 1). Because of the considerable hazard it poses to densely populated areas in California (Jones et al., 2008), the SSAF has been extensively studied using geologic, geophysical, geodetic, and other kinds of data. The SSAF has not produced a major event in historic times (over the last ~300 years; Philibosian et al., 2011), and is currently believed to pose the largest seismic hazard in California (Field et al., 2014). Despite significant progress made toward understanding the

Investigation: Ellis J. Vavra, Hongrui Qiu, Benxin Chi, Pieter-Ewald Share, Amir Allam, Frank Vernon, Yehuda Ben-Zion, Yuri Fialko

Methodology: Ellis J. Vavra, Hongrui Qiu, Benxin Chi, Pieter-Ewald Share, Yehuda Ben-Zion, Yuri Fialko

Project Administration: Yehuda Ben-Zion, Yuri Fialko

Resources: Amir Allam, Yuri Fialko

Software: Ellis J. Vavra, Hongrui Qiu, Benxin Chi, Pieter-Ewald Share, Yuri Fialko

Supervision: Yehuda Ben-Zion, Yuri Fialko

Validation: Ellis J. Vavra, Hongrui Qiu, Benxin Chi, Pieter-Ewald Share, Yuri Fialko

Visualization: Ellis J. Vavra, Hongrui Qiu, Benxin Chi, Pieter-Ewald Share, Yuri Fialko

Writing – original draft: Ellis J. Vavra, Hongrui Qiu, Benxin Chi, Yehuda Ben-Zion, Yuri Fialko

Writing – review & editing: Ellis J. Vavra, Hongrui Qiu, Benxin Chi, Pieter-Ewald Share, Amir Allam, Matthias Morzfeld, Frank Vernon, Yehuda Ben-Zion, Yuri Fialko

properties and seismic potential of the SSAF, several important questions remain. While the surface trace of the SSAF in the Coachella Valley is reasonably well known based on geologic, geomorphologic, and geodetic data (Allen et al., 1972; Lindsey, Fialko, et al., 2014; Sieh & Williams, 1990; Tymofyeyeva et al., 2019), the sub-surface fault geometry is a matter of debate. A classic model of a vertical strike-slip fault is commonly assumed (Anderson, 1951; Shaw et al., 2015). However, numerous lines of evidence have emerged that challenge this model and instead suggest that the SSAF has a northeast dip of 60–70°. The locus of seismicity (Lin et al., 2007) and maximum interseismic strain rate (Fialko, 2006; Lindsey & Fialko, 2013; Tymofyeyeva & Fialko, 2018) are offset to the northeast of the fault trace. Seismic imaging studies have observed dipping reflectors in the upper crust (Fuis et al., 2017; Persaud, 2016) and dipping contrasts in seismic velocities that possibly extend into the lower crust and upper mantle (Ajala et al., 2019; Fuis et al., 2012; Share et al., 2019; Zigone et al., 2015). Locally observed fault-zone head-waves have been interpreted as requiring a dipping bimaterial interface (Share & Ben-Zion, 2016). Models of potential field data suggest a moderate fault dip of 50–70° in the mid-upper crust (Fuis et al., 2017; Langenheim & Fuis, 2022). Studies of regional seismic anisotropy revealed a northeast-dipping tectonic fabric (Schulte-Pelkum et al., 2020). Numerical models of long-term fault slip further suggest that a northeast-dipping SSAF is required to produce the observed uplift and subsidence patterns along the fault (Fattaruso et al., 2014).

A region of dipping seismicity over a depth interval of ∼5–10 km (Lin et al., 2007; Lindsey & Fialko, 2013) is perhaps the most direct evidence of an active fault structure. However, it remains unclear if this structure represents the main SSAF interface that accommodated tens to hundreds of kilometers of relative displacements and is likely to rupture during the next major earthquake, or whether it represents a subsidiary fault with minor offset. Similarly, it is uncertain whether the inferred dipping structure connects to the surface trace of the SSAF. Insights from precisely located seismicity are unfortunately limited because of relatively low seismicity rates and a narrow range of hypocentral depths (∼5–10 km; Lin et al., 2007; Ross et al., 2019; Schulte-Pelkum et al., 2020) due to the predominantly aseismic behavior of the shallow section of the SSAF, which is known to creep in the interseismic period (Allen et al., 1972; Lindsey, Fialko, et al., 2014; Sieh & Williams, 1990; Tymofyeyeva et al., 2019). Measurements of interseismic deformation are also limited in this regard because they are only sensitive to the fault location at the bottom of the seismogenic zone (Fialko, 2006). For these reasons, imaging the shallow (<5 km) geometry of the SSAF is critical for understanding the fault configuration throughout the upper crust.

In this study, we use a combination of space geodetic and seismic observations, along with inverse modeling, to resolve the subsurface geometry of the SSAF. In particular, we use Interferometric Synthetic Aperture Radar (InSAR) to measure surface displacements due to shallow creep and invert them for the fault dip angle in the shallow (top 2–3 km) aseismic crust. To image the fault zone structure in the same depth interval independently, we deployed a dense array of seismic stations across the SSAF north of the extent of observed creep, near Thousand Palms (Figure 1). We implement a novel reverse-time migration procedure (Qiu et al., 2023) to analyze the structure of the shallow fault damage zones associated with the Banning and Mission Creek strands of the SSAF. Finally, we compare the newly derived constraints on the near-surface fault orientation to each other, as well as to other available data, and present a unified description of subsurface geometry of the SSAF throughout the upper crust.

2. Surface Deformation Due To Shallow Fault Creep

We make use of surface deformation due to shallow creep to evaluate the fault attitude near the Earth's surface. The decay of surface velocities away from the fault trace is indicative of the depth extent of shallow creep, as well as the fault dip angle. In the case of a non-vertical slip interface, surface velocities are expected to be larger on the hanging wall side of the fault (Fialko, 2004; Segall & Lisowski, 1990). Measuring the velocities associated with creep is challenging because they are small - on the order of millimeters per year (Lindsey, Fialko, et al., 2014; Tymofyeyeva et al., 2019) - and superimposed on a longer-wavelength deformation signal due to the relative plate motion below the brittle-ductile transition (Bennett et al., 1996; Fialko, 2006; Johnson et al., 1994; Lindsey & Fialko, 2013). We use InSAR to map deformation associated with the SSAF and isolate the signal due to shallow creep by subtracting a model of regional secular deformation constrained by the Global Navigation Satellite System (GNSS) data (Bock et al., 2017; Herring et al., 2016).
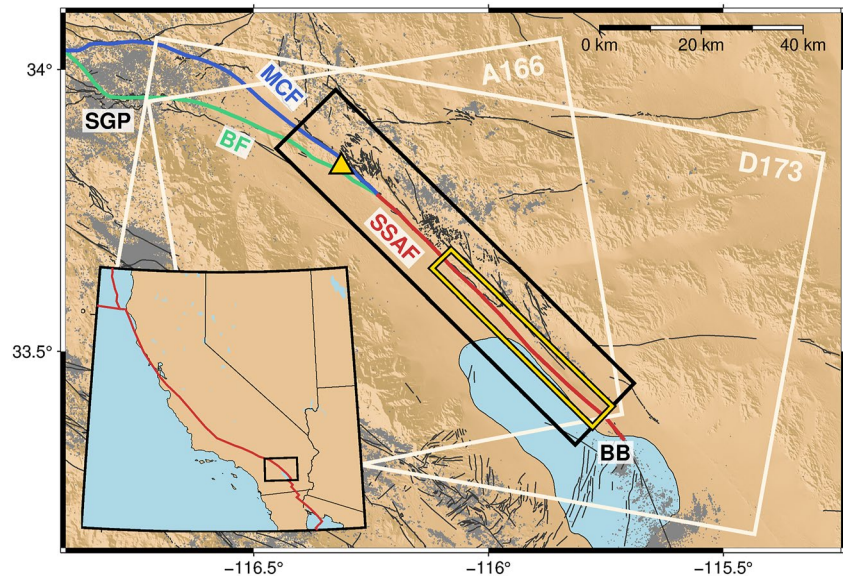
Figure 1. Tectonic setting of Southern San Andreas Fault overlain on shaded-relief topography (Farr et al., 2007). The Southern San Andreas Fault (SSAF), Mission Creek Fault (MCF), and Banning Fault (BF) are highlighted in red, blue, and green, respectively. Other Quaternary faults are denoted by black curvy lines (USGS, 2020). The locations of San Gorgonio Pass (SGP) and Bombay Beach (BB) are labeled. Gray dots denote epicenters of local earthquakes (Ross et al., 2019). The yellow triangle denotes the location of the temporary seismic array. White rectangles show the footprint of Sentinel-1 SAR satellites' ascending track 166 and descending track 173. The black rectangle outlines the area of Figure 3, where shallow creep is observed. The yellow box indicates an area used for inverse modeling of surface displacements. The inset shows the regional location of the main figure (black box) and the boundary between the Pacific and North American plates (red line).

2.1. InSAR Data Processing

We utilized a well-populated catalog of SAR data from the European Space Agency's Sentinel-1 satellites (Torres et al., 2012), and processed all data acquired between 2014 and 2022 from the ascending track 166 and descending track 173 (Figure 1). The data were acquired in the Terrain Observation by Progressive Scan (TOPS) mode in C-band (radar wavelength of 56 mm), and processed using GMTSAR (Sandwell et al., 2011). We co-registered each set of SAR images using the Bivariate Enhanced Spectral Diversity (BESD) method (Wang et al., 2017). Each TOPS image consists of three sub-swathes; we used sub-swath 1 from the ascending track 166 and sub-swathes 2 and 3 from the descending track 173 that cover the area of interest (see Figure 1 and Figure S1 in Supporting Information S1). We formed interferometric pairs between all sequential acquisitions, as well between every-other ("skip-1") acquisition. The topographic contribution to the radar phase was calculated and removed using digital elevation data from the TanDEM-X DEM that has resolution of 12 m (Rizzoli et al., 2017).

It is known that multi-looking and filtering of interferograms introduces a systematic bias that can affect the accuracy of deformation measurements (Lau et al., 2018; Maghsoudi et al., 2022; Michaelides et al., 2019; Tymofyeyeva et al., 2019; Zheng et al., 2022). We use the unfiltering method (Tymofyeyeva et al., 2019) to identify stable pixels and prevent a systematic accumulation of decorrelation noise. In particular, we take the difference between the filtered and raw wrapped phase (modulo 2π) and subtract it from the filtered unwrapped phase up-sampled to full resolution. The resulting unfiltered unwrapped phase ensures zero circuit closure if the noise (including errors introduced by filtering) is smaller than $\pm\pi$ radians. Pixels that do not satisfy this condition are subject to the 2π phase ambiguity errors equivalent to the phase unwrapping errors. We identify and mask out such pixels using circuit closure analysis (Tymofyeyeva et al., 2019). The remaining set of stable pixels is common to all interferometric pairs, and can be multi-looked without violating the circuit closure condition. To improve the signal-to-noise ratio, in each multi-look cell we weigh contributions of pixels using the amplitude dispersion (Ferretti et al., 2001; Hooper et al., 2004). This enhances the contribution from stable scatterers. We then perform common scene stacking to correct for atmospheric noise (Tymofyeyeva & Fialko, 2015).

We compute the time series of line-of-sight (LOS) displacements at every coherent pixel by summing the phase of sequential interferograms corrected for decorrelation and atmospheric noise. We then estimated the average
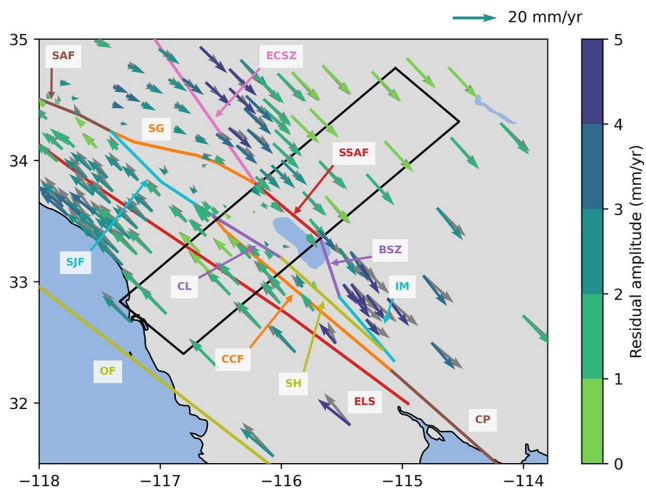
Figure 2. Horizontal surface velocities derived from regional GNSS measurements. We use 154 sites which passed quality control (see Section 2.2). The observed velocities (gray arrows) are compared with predictions of the best-fitting regional tectonic deformation model (blue-green arrows). The color scale of the model predictions corresponds to the amplitude of their residual vectors and is saturated at 5 mm/yr. The average residual within the plate boundary-perpendicular swath (black box) is subtracted from the model prediction in order to account for errors in the reference frame correction due to model residuals away from the primary area of interest. Model residuals within the swath are within 1.3 ± 0.7 mm/yr and 2.2 ± 1.1 mm/yr for the entire region. Straight color lines denote locations of modeled faults at the bottom of the seismogenic zone. The modeled fault segments are the Brawley Seismic Zone (BSZ), Cerro Prieto Fault (CP), Clark Fault (CL), Coyote Creek Fault (CCF), Eastern California Shear Zone (ECSZ), Elsinore Fault (ELS), Imperial Fault (IM), Offshore Fault (OF), San Andreas Fault (SAF), San Jacinto Fault (SJF), San Gorgonio Fault (SG), Southern San Andreas Fault (SSAF), and Superstition Hills Fault (SH).

LOS velocities for the time period between 1 May 2017 and 1 November 2021 by fitting a spline to the displacement time series for each pixel, differencing the spline values corresponding to the chosen dates, and dividing the difference by the respective time interval (4.5 years) (Figure S1 in Supporting Information S1). We do not use a longer time period to compute creep velocities because (a) little or no shallow creep occurred between 2014 and mid-2017 (Tymofyeyeva et al., 2019), and (b) no data were collected from the ascending track 166 following a malfunction of the Sentinel-1B satellite in December of 2021.

2.2. Isolating Deformation Due To Shallow Creep

The resulting LOS velocity maps primarily reflect deformation due to secular tectonic deformation; however, shallow creep is evident from the discontinuity in velocity across the SSAF trace (Figure S1 in Supporting Information S1). To extract the short-wavelength deformation signal associated with shallow creep, we estimated the long-wavelength interseismic velocity field using a regional fault model constrained by continuous GNSS data from the Scripps Orbit and Permanent Array Center (Bock et al., 2017) and Earthscope Consortium (formerly UNAVCO) (Herring et al., 2016). The GNSS data set consisted of 236 continuous GNSS sites within the study area (Figure 2) that were operational between 2013 and 2022 (i.e., coincident with the Sentinel-1 InSAR acquisitions). In an initial quality check, we excluded sites that had data gaps cumulatively exceeding 3 years, or exhibited highly irregular displacement time series, reducing the final data set to 154 stations (see Supporting Information for lists of used and excluded GNSS sites). For each component of the horizontal displacement (i.e., east and north), we detrended the time series by removing the best linear fit. We then removed the outliers and offsets from the residual, added back the previously subtracted slope, and re-estimated the best linear fit (Fialko & Jin, 2021). Because a number of sites in the target area were affected by co- and post-seismic deformation due to the 2019 Ridgecrest earthquakes (Jin & Fialko, 2020), we estimated the interseismic velocities using data up to 1 July 2019. The resulting secular velocities are shown in Figure 2 (gray arrows). To generate a high-resolution model of secular velocities that is not sensitive to local site effects and possible interpolation errors, we inverted the GNSS velocities using a three-dimensional (3-D) regional fault model.

We adopt the fault geometry model of Tymofyeyeva and Fialko (2018) that was constrained by seismicity and Quaternary fault traces. This model includes several segments of the San Andreas and San Jacinto fault systems, as well as the Elsinore, Imperial, Cerro Prieto faults, and the Eastern California Shear Zone (2, Table S1 in Supporting Information S1). In addition, we include an extra fault (OF) representing off-shore deformation associated with faults in the California Borderland (Platt & Becker, 2010). Each fault is represented by a finite rectangular dislocation (Okada, 1985) with an upper edge located at the inferred locking depth corresponding to the bottom of the seismogenic zone. The lower dislocation edge is at 10^4 km depth (i.e., large enough to approximate a semi-infinite dislocation). The upper edges of the respective dislocations are shown in Figure 2 (gray lines) and the assumed locking depths are listed in Table S1 in Supporting Information S1. By considering the location of seismicity at depth rather than the fault traces at the surface, we account for a possible non-vertical orientation of some of the faults in the seismogenic zone.

We solve for slip rates on faults in the immediate proximity to the Coachella-Imperial Valley region; slip rates on the remaining ("far-field") faults are fixed based on the slip rates in Tymofyeyeva and Fialko (2018) (see Table S1 in Supporting Information S1). We additionally constrain the slip rates on the SSAF-Brawley Seismic Zone, and Clark-Superstition Hills segments to be equal (Tymofyeyeva & Fialko, 2018). The surface velocity is calculated by superimposing contributions from individual fault segments. We invert the interseismic velocity field (Figure 2) for the slip rates on the SSAF-Brawley Seismic Zone, Coyote Creek, and Clark-Superstition Hills segments. Because the fault geometry is fixed, the inverse problem is linear, and can be solved using least squares.
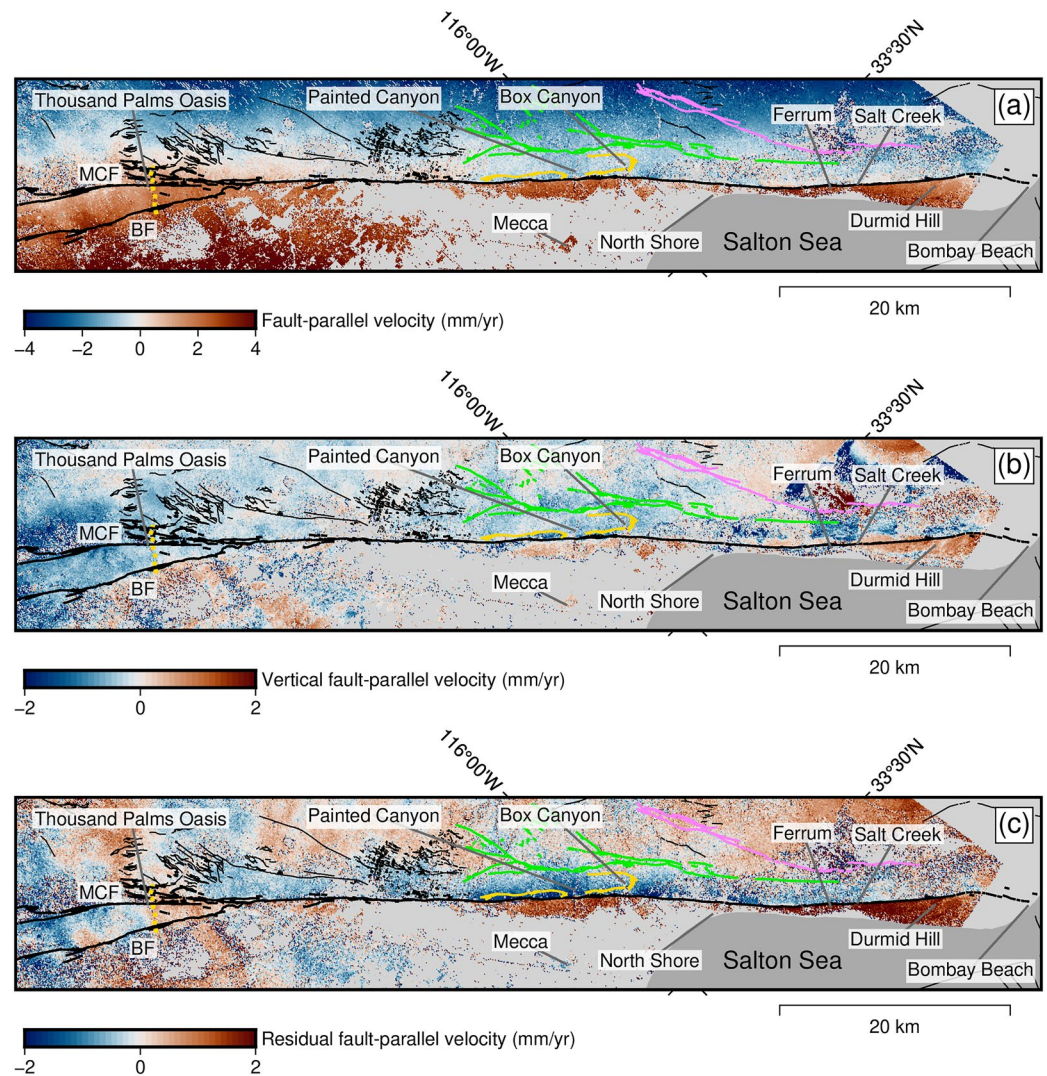
Figure 3. (a) Horizontal fault-parallel velocity field derived from Sentinel-1 InSAR data (Figure S1 in Supporting Information S1). Positive velocity (red color) corresponds to northwest motion and negative velocity (blue color) corresponds to southeast motion. The thick black line corresponds to the San Andreas Fault (SAF). The Skeleton Canyon (yellow), Mecca Hills (green), and Hidden Spring (magenta) fault zones are also highlighted. Thin black lines denote other Quaternary faults (USGS, 2020). The velocity contrast along the trace of the San Andreas Fault is indicative of shallow creep. The thick dashed yellow line denotes the seismic array location. (b) Vertical velocity derived from Sentinel-1 InSAR data. Positive velocity (red color) corresponds to uplift and negative velocity (blue color) corresponds to subsidence. (c) Residual fault-parallel velocity obtained by subtracting the GNSS-constrained long-wavelength secular velocity (Figure 2) from the InSAR-derived fault-parallel velocity shown in panel (a). Sign of residual velocities is the same as (a).

In addition to the fault slip rates, we solve for a rigid body translation to account for the relative nature of the reference frame. After performing the initial least squares fit, we update the rigid body translation by subtracting the mean residual of stations within a SSAF-perpendicular profile (black rectangle, Figure 2) from the model predictions. The inverted slip rates are in general agreement with those of Tymofyeyeva and Fialko (2018), with some minor differences. The new slip rate is ~3 mm/yr lower for the Clark-Superstition Hills faults, and ~2 mm/yr higher for the SSAF-Brawley Seismic Zone and Coyote Creek fault. These differences likely stem from different input data and the addition of a fault representing offshore deformation.

Velocities from the best-fit model are shown in Figure 2 (arrows, color-coded by the misfit magnitude). As can be seen in Figure 2, there is good agreement between the data and model predictions in the area of interest around the SSAF. A slightly worse fit in other regions is likely due to an over-simplified or less-constrained model geometry (e.g., in the Imperial Valley and ECSZ) in combination with the near-field rigid body translation adjust-
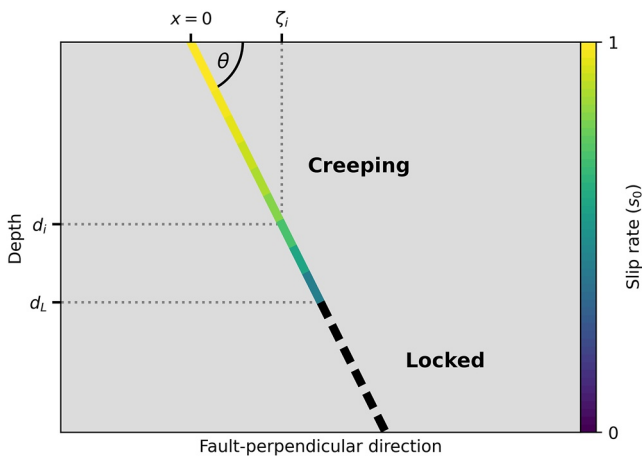
Figure 4. Schematic diagram of the geometry of the 2D dislocation model. The creeping portion near the surface is discretized into L finite patches. Slip rate is assumed to have a semi-elliptical distribution, tapering to zero toward shallow locking depth d_L (Equation 1). Below d_L, the fault is assumed to be locked. Other geometric parameters from Equations 2 and 3 are also shown. An example illustrated in the figure assumes $\theta = 60°$ and $L = 10$. In our inversions, we use $L = 20$.

ment. Our assumptions of pure strike-slip motion and uniform slip rate along each segment may also contribute to model misfits. Within the profile, model residuals are on average 1.3 ± 0.7 mm/yr, with only several stations having misfit greater than 2 mm/yr. These stations are located at the northern and southern boundaries of the modeled domain where the assumed geometry of an active fault system is likely oversimplified.

We used the best-fit fault model to calculate the east and north components of surface velocity on a spatially dense grid with a uniform resolution of 200 m. We then projected the calculated surface velocities into the satellite LOS for each satellite track, assuming that the vertical secular motion is negligible (<1 mm/yr), which is indicated by secular crustal velocities (Shen et al., 2011). The observed LOS velocities were adjusted to agree with the modeled ones at wavelengths greater than 20 km using the SURF method (Tong et al., 2013).

Assuming an average fault strike of $\alpha = 315°$, we then combined the LOS velocities from the ascending and descending orbits to obtain the fault-parallel (Figure 3a) and vertical (Figure 3b) velocity components (for details, see Lindsey, Fialko, et al., 2014; Lindsey & Fialko, 2016; Tymofyeyeva & Fialko, 2018). Finally, we subtracted the modeled fault-parallel velocity constrained by GNSS data from the InSAR-derived velocity (Figure 3a) to obtain the residual velocity due to shallow fault creep (Figure 3c).

The residual velocity field features a discontinuous anomaly due to shallow creep on the SSAF that extends from Bombay Beach at the south to the bifurcation of the SSAF into the Mission Creek Fault and Banning Fault segments to the north (Figure 3). A comparison with surface displacements that occurred due to a dynamically triggered slow slip event between 2017 and 2019 (Tymofyeyeva et al., 2019) indicates that shallow creep propagated at least 10 km further north of Painted Canyon and as well as several kilometers south of Durmid Hill toward Bombay Beach over the subsequent 2 years.

Several features are notable in the vertical velocity field (Figure 3b). Northeast of Salt Creek ($y < 10$ km), there is complex vertical deformation caused by hydrological processes associated with the Coachella Canal (Figure 3b). This deformation has been reported in previous InSAR studies and can be attributed to groundwater extraction/recharge due to canal leakage (Lindsey, Fialko, et al., 2014; Lyons & Sandwell, 2003). Several regions of uplift are apparent between Box Canyon and North Shore, as well as in the vicinity of Durmid Hill. The Durmid Hill uplift signifies a long-term transpressional deformation (Bürgmann, 1991; Lindsey, Fialko, et al., 2014). Other signals are likely related to local hydrology. Lindsey, Fialko, et al. (2014) detected a differential subsidence across the fault (west side down) at Painted Canyon, where our more recent data indicate an uplift (Figure 3b). This reversal could result, for example, from a partial recharge of aquifers in Coachella Valley. It is known that faults can act as hydrologic barriers, and produce highly localized differential vertical motion due to changes in pore pressure or fluid saturation at depth (Bawden et al., 2001; Chaussard et al., 2014).

2.3. Forward Modeling of Shallow Creep

To interpret the InSAR observations of shallow creep, we use a two-dimensional (2D) fault model based on a superposition of screw dislocations (Segall, 2010). While the surface trace of the SSAF exhibits some undulations on a scale of tens of kilometers (Bilham & Williams, 1985; Lindsey, Fialko, et al., 2014; Tymofyeyeva et al., 2019), it is quasi-linear on shorter scales of the order of several kilometers. Provided that the rate and depth extent of shallow creep do not substantially vary along strike on distances smaller than several kilometers (as we demonstrate below), anti-plane strain can be assumed and the 2D approximation is valid. For simplicity, we assume that the upper fault section that accommodates shallow creep is planar and characterized by a dip angle θ (Figure 4) which is allowed to gradually change in the along-strike direction.

Physics-based models of shallow creep require that the creep rate decreases toward the nominally locked deeper "seismogenic" section (Kaneko et al., 2013; Lindsey & Fialko, 2016). Because surface displacements are relatively insensitive to the details of slip tapering at depth (Lindsey, Sahakian, et al., 2014; Mavko, 1981),

we assume a semi-elliptical displacement profile (see Equation 1 and Figure 4) that corresponds to a constant stress drop (Fialko, 2007). Fault slip is approximated by a superposition of L screw dislocations extending from the surface to the shallow locking depth d_L. The assumed semi-elliptical slip distribution s_i as a function of a depth d_i is given by

$$s_i(d_i) = s_0 \sqrt{1 - (d_i/d_L)^2} \quad \text{for } i = 0, \ldots, L-1 \tag{1}$$

where s_0 is the slip at the Earth's surface (Figure 4). To characterize possible along-strike variations, we consider surface displacements from a number of profiles that are regularly spaced along the fault strike. At any given along-strike coordinate y, the surface displacement D as a function of distance to the fault trace x is:

$$\begin{aligned}
D(x, s_0, d_L, \theta) = & \; \frac{s_0}{\pi} \left[\frac{\text{sgn}(x)}{2} - \arctan\left(\frac{x - \zeta_0}{d_0} \right) \right] \\
& - \sum_{i=1}^{L-1} \frac{s_i}{\pi} \left[\arctan\left(\frac{x - \zeta_i}{d_i} \right) - \arctan\left(\frac{x - \zeta_{i-1}}{d_{i-1}} \right) \right]
\end{aligned} \tag{2}$$

where ζ_i is the offset of the ith dislocation from the fault trace ($x = 0$) due to the fault dip (Figure 4),

$$\zeta_i = \frac{d_i}{\tan \theta}. \tag{3}$$

The larger the number of dislocations L, the more accurately the superposition of dislocations approximates the elliptical slip profile. To determine an appropriate value of L, we performed sensitivity tests in which we computed the net change in the predicted displacements ΔD for models with increasing L for different fault dip angles θ. The value of L most significantly impacts hanging-wall deformation in non-vertical fault geometries. Increasing L to 10 accounts for nearly all the deformation predicted by models with $L = 100$ — improvements in the model approximation amount to <1.5% for $L > 10$. Since typical error estimates from data down-sampling InSAR profiles are on the order of several mm/yr, and rarely less than 0.5 mm/yr (Figure 5), $L = 10$ should provide sufficient discretization. We use $L = 20$ in our calculations to ensure satisfactory precision.

In order to compute surface velocities v, the displacements are divided by the observation time span t, $v = D/t$. Because of a limited aperture of the observation profiles and possible residual errors in the surface velocity data, the velocity profile may not asymptote to 0 for $x \gg d_L$. To limit the extent to which this effect could bias our results, we included a "nuisance parameter" v_c to account for a constant velocity shift such that the final form of the forward model is $v(x) = D(x)/t + v_c$. The effects of this parameterization are discussed in Section 2.5.

2.4. Inversions for Shallow Fault Geometry and Creep Rate

We perform a series of inversions using the 2D dislocation model to estimate the local slip rate and fault geometry along the creeping portion of the SSAF. To capture possible variations in the fault geometry and shallow slip rate, we place 20 km-by-1 km fault-perpendicular profiles every 1 km along the fault trace (Figure S2 in Supporting Information S1; see list of sites in Supporting Information). Because phase decorrelation limits the spatial coverage of the creep signal (Figure 3) and results in irregular data gaps near the fault, we complement data from a given 1 km-wide velocity profile with data from adjacent profiles (Figure S2 in Supporting Information S1).

We apply logarithmic down-sampling to the data points within each profile to increase the spacing between the samples away from the fault trace, where variations in surface velocity are expected to decrease (Figures 5a–5c). Downsampled data from each profile are assigned a weight b based off of their along-strike distance to the main profile (Figure S2 in Supporting Information S1). The main profile is assigned a weight of 1, and adjacent profiles are assigned weights that decrease with increasing along-strike distance from the main profile, in a Gaussian-like fashion (Figure S2 in Supporting Information S1). The Gaussian weighting kernel has a spatial wavelength of 2 km. The three adjacent up- and down-strike profiles are included in each inversion for the 2D fault geometry at the location of the main profile (Figure S2 in Supporting Information S1). We compute the variance σ^2 of the data used in each down-sampling bin, which are aggregated to form a diagonal covariance matrix Σ to be used in the likelihood function (Equation A3; see Appendix A). To reduce biases introduced by noisy regions of the velocity map, we require that at least five pixels are used in each bin average and that their standard deviation σ is less or equal to 10 mm/yr; all down-sampled data which do not meet these criteria are discarded.
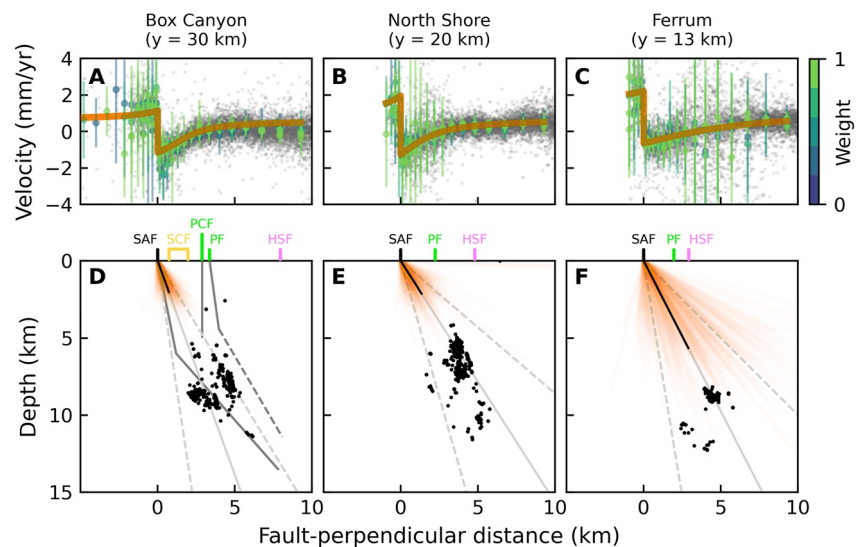
Figure 5. Shallow fault geometry from geodetic modeling and precisely located earthquake hypocenters. (a–c) Observed (gray points), down-sampled (blue-green points and error bars), and modeled (orange curves) velocity profiles from several locations along the fault. The color of the down-sampled data corresponds to their weight in the inversion, where green indicates high weight and blue indicates low weight. Uncertainties for each down-sampled point are the standard deviation of the original points. (d–f) Cross-section comparison between fault geometries (orange lines) computed from the estimated values of fault dip θ and shallow locking depth d_L and earthquake hypocenters (black points). The locations of subsidiary faults to the northeast of the SSAF are marked and labeled (USGS, 2020), with colors the same as Figure 3. We show 500 random samples from the ensemble of shallow fault geometries obtained through the Bayesian inversion, plotted with transparency to illustrate regions of high-likelihood. The same ensemble samples from (a–c) are shown in (d–f). The geometry from the average dip θ and shallow locking depth d_L and is shown in black. The fault geometries of Fuis et al. (2017) are shown in dark gray. Earthquake hypocenters are selected using 20-km-by-6-km swaths centered at the given fault location. Dashed light gray lines show the projection of shallow fault dip angles to seismogenic depth in the crust, derived from the 1σ-uncertainty in the estimated fault dips. The solid gray line representing the mean. Each column corresponds to a particular along-fault coordinate y (zero is −115.760754° longitude/33.389494° latitude), measured north from Bombay Beach.

Our inversions implement a Bayesian Markov chain Monte Carlo (MCMC) scheme to estimate the best-fitting model parameters, as well as characterize their uncertainties. The sampling algorithm explores the model parameter space in a stochastic manner, drawing samples guided by a likelihood (i.e., cost) function and prior distribution (i.e., a priori information). By generating an ensemble of models which can reasonably explain the data, we can attempt to quantify the uncertainty of our inversions.

We define a Gaussian likelihood function that incorporates model misfits, estimated data uncertainties, and spatial data weights (Equation A3) and draw samples from the posterior distribution using an affine invariant ensemble sampler (Foreman-Mackey et al., 2013). To restrict the amount of a priori information included with respect to the fault structure, we impose a uniform prior distribution informed only by general physical constraints on fault geometry and slip. We allow the fault dip θ to vary from 0 to 180° and shallow locking depth d_L from 0 to 15 km. Dip angles $\theta < 90°$ correspond to a northeast dip and $\theta > 90°$ corresponds to a southwest dip. Inspection of the velocity profiles suggests that the surface slip rate v_0 is of the order of a few mm/yr. Correspondingly, we permit a range of slip rates from 0 to 10 mm/yr. In order to ensure that the nuisance parameter v_c is only accounting for errors in the InSAR data, we select its prior bounds based on the long-wavelength deformation misfits. The amplitude of residuals near the fault are typically <2 mm/yr (Figure 2), so we limit the range of v_c to ±2 mm/yr. Additional details of the Bayesian framework and MCMC implementation are described in Appendix A.

2.5. Evaluating Long-Wavelength Deformation Corrections

Given the localized and low-amplitude nature of deformation associated with fault creep (Figure 3), we performed a series of tests to explore how the modeling results depend on various choices made in the data processing and model parameterization. Specifically, we explored to what extent the inferred best-fit parameters are affected by the filter wavelength in the SURF correction (Tong et al., 2013), as well as the velocity nuisance parameter v_c
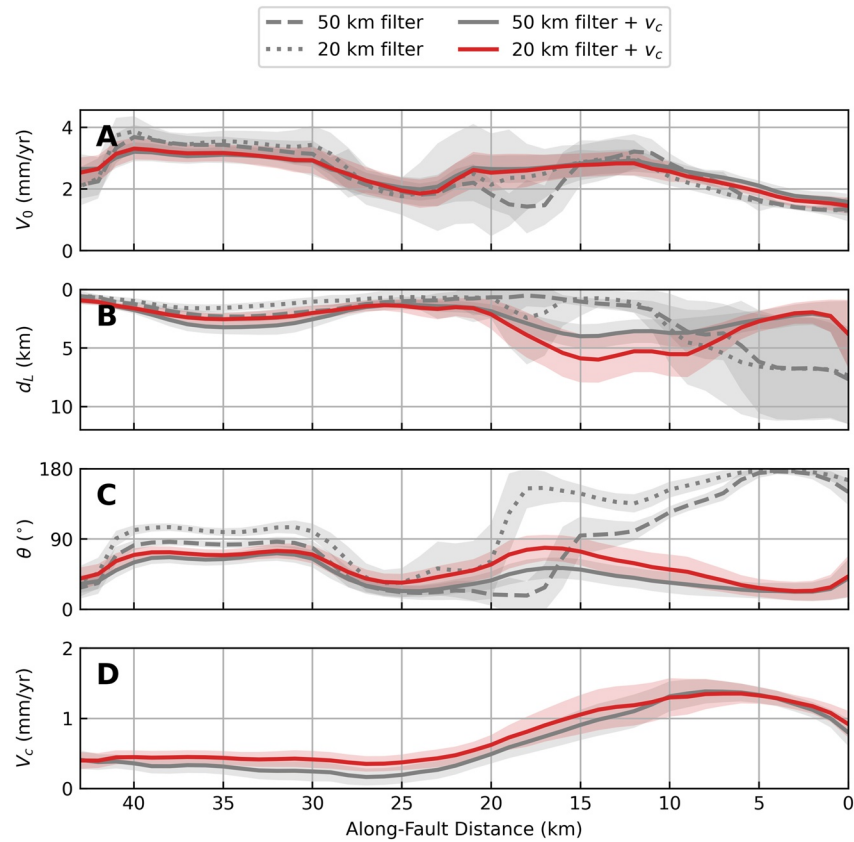
Figure 6. Comparison of the effects of high-pass filter wavelength and inclusion of a constant velocity shift v_c on inversions for surface slip rate v_0, shallow locking depth d_L, and fault dip θ. Shaded regions indicate 1σ uncertainty estimates obtained from the Bayesian inversions. Without narrow limits on allowed θ, inversions that exclude v_c tend toward unrealistic dip values at the southern end of the fault ($x = 0$ km) and contain more drastic parameter changes along-strike. The red curve corresponds to the corrections ultimately used in analysis (20 km high-pass filter, velocity shift v_c included). Zero is at $-115.760754°$ longitude/$33.389494°$ latitude.

(see Section 2.3). The SURF procedure ensures that InSAR measurements are consistent with long-wavelength deformation observed by GNSS. First, a long-wavelength velocity field from GNSS is removed from the InSAR velocity field—in our case, the former is derived from a fault model, but could instead be from interpolated GNSS measurements. This leaves a residual velocity field, which is high-pass filtered to remove possible long-wavelength artifacts while preserving smaller-scale features (e.g., due to fault slip). The initially removed long-wavelength velocity is then added back to the high-pass filtered data. For our tests, we used filter wavelengths of 20 and 50 km for the SURF correction. We then performed two separate inversions for each data set: one including and one excluding the v_c parameter (see Section 2.3 and 2.4).

The corresponding inversion results are shown in Figure 6. Surface slip rate v_0 is least dependent on the considered model assumptions (Figure 6a). The shallow locking depth d_L and dip angle θ are weakly dependent on the model assumptions in the northern part of the fault ($y > 20$ km), but exhibit considerable variability in the southern part due to a limited data coverage on the southwest side of the fault, and higher noise levels on the northeast side. The results from both inversions without v_c exhibit large excursions and unrealistic variations in the dip value over length scales of <5 km (Figure 6c). The models with v_c included are better able to account for non-zero asymptotic behavior and consequently produce models generally confined to a range of physically-reasonable dip estimates. Thus, we conclude that including v_c as a free parameter helps produce more accurate inferences of the shallow fault geometry and shallow locking depth.

To independently evaluate which degree of filtering is more appropriate, we compute the weighted root-mean-square error (wRMSE) for each set of modeled profiles,
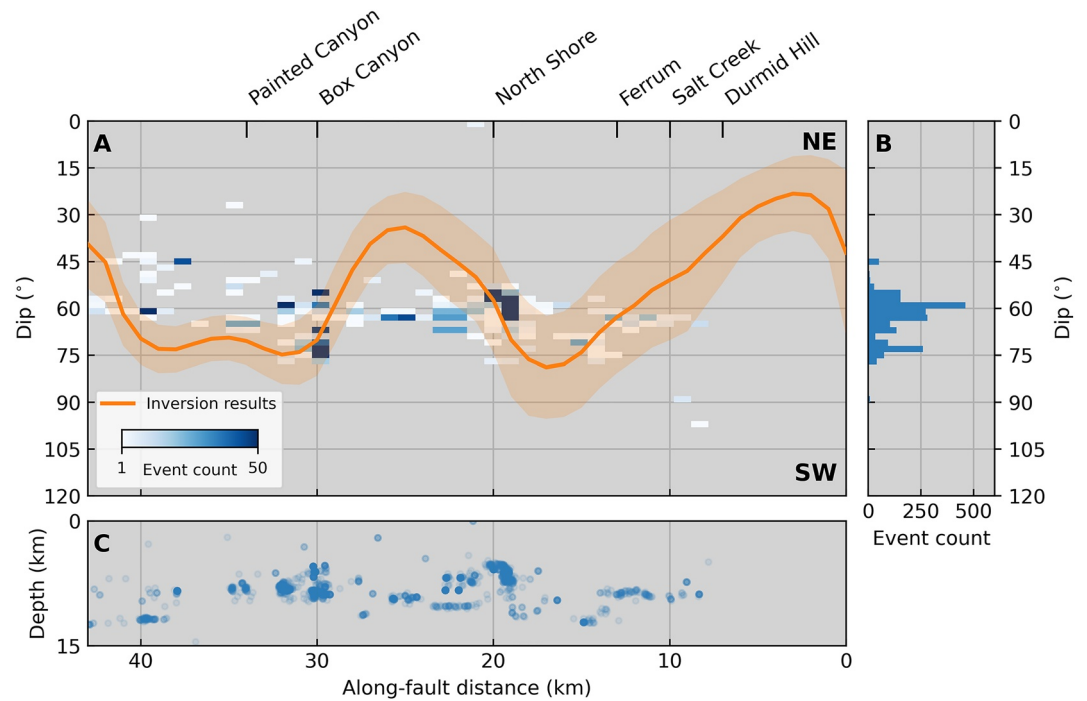
Figure 7. Comparison of fault dip estimates from InSAR and earthquake hypocenters. (a) Along-strike variation in dip estimates. Geodetic inversion results are overlain on a 2D histogram of dip angles estimated from 2008 to 2017 seismicity locations from the Caltech quake template matching catalog (Ross et al., 2019). We select earthquakes from the same 20 km-by-1 km swaths used in the geodetic inversions and compute dip angles θ assuming that each event is located on a plane connecting to the SSAF surface trace. We average estimates of θ into 3° bins and only show bins which include at least one event. Compass schematically indicates sense-of-dip (NE vs. SW) and strike direction (NW). (b) Histogram of all dip estimates derived from seismicity. (c) Fault-perpendicular projection of events used to estimate local fault dip in (a). Some events appear multiple times in (c) due to changes in fault strike and subsequent overlap in swaths. Zero is at −115.760754° longitude/33.389494° latitude.

$$\text{wRMSE} = \left[\frac{1}{N} \sum_{i=0}^{N} \frac{b_i(d_i - v_i(m))}{\sigma_i^2} \right]^{1/2} \qquad (4)$$

where N is the number of binned profile data, d_i are the bin averages, $v_i(m)$ is the model prediction using the mean parameter values m obtained from the Bayesian inversion, σ_i are bin standard deviations, and b_i are the data weights specified by the along-strike weighting kernel. Note that this is proportional to the log-likelihood function used in the Bayesian inversion (see Equation A3). We point out that the wRMSE is only sensitive to high-frequency spatial noise and thus is valid for comparing models derived from data sets that differ only in their long-wavelength components.

We find that the wRMSE values from the 20 km filtered data set generally are similar to or less than those of the 50 km filtered data set (Figure S4 in Supporting Information S1). The most significant difference between the fault geometry estimates is that the 20 km filtered model exhibits 10– 20° steeper dip angles θ over the central section of the fault (Figure 6c), which results in better correspondence with the location of seismicity near the fault (Figure 7). Through combination of these considerations, we determine that the shorter-wavelength 20 km filter is more appropriate for isolating the deformation signal due to shallow fault creep.

2.6. Results

In a set of trial inversions, we found that a surface slip rate less than ~1 mm/yr results in a signal-to-noise ratio that is too small for a reliable recovery of the model parameters. Therefore, we only inverted data from a ~40 km

long section of the fault where the surface slip rate is sufficiently large ($v_0 \geq 1$ mm/yr) and the velocity data are available on both sides of the fault (see Figure 3).

The best-fit models consistently indicate an average surface slip rate of ~2–4 mm/yr and a depth extent of creep of 1–5 km along most of the SSAF (Figures 6a and 6b). Notably, the models prefer a shallow-to-steep northeast dip of the entire shallow part of the SSAF involved in aseismic slip (Figures 5 and 6). One location where a vertical dip might be allowed by the geodetic data is around the along-strike coordinate $y \approx 17 \pm 2$ km, south of the Salton Sea's North Shore (Figures 6 and 7), but only at the high end of the estimated uncertainties on the fault dip angle θ. To test the null hypothesis of a vertical fault, we performed the same inversion with a fixed dip angle $\theta = 90°$. The assumption of a vertical fault produces higher wRMSE values at all locations along the fault (Figure S3 in Supporting Information S1), confirming the northeast dipping geometry is preferred.

At some locations, the inverse models with unconstrained θ suggest a dip angle of ~30–50° (Figure 7). While we cannot exclude such a possibility, we note that the data quality at these locations is somewhat degraded due to reduced radar coherence (which gives rise to a higher data scatter and a lower signal-to-noise ratio), insufficient coverage on the southwest side of the fault (due to a close proximity to the Salton Sea or agricultural areas in the Coachella Valley), or both. It also is possible that vertical signals may leak into the fault-parallel component of motion (see Section 2.2) or reflect more complex deformation than is captured by our 2D modeling (i.e., south of Salt Creek, Figure 3b). We therefore do not consider the shallowest dip angles to be a robust feature of our inverse models.

3. Shallow Structure From Reverse Time Migration Analysis

3.1. Large-N Seismic Array

To directly image the fault zone geometry in the uppermost crust, we deployed a dense (>300 nodes) seismic array along Thousand Palms Canyon, where the surface creep tapers off (Figure 3) and the SSAF bifurcates into the Mission Creek and Banning segments (Figures 1 and 8). The deployment included a 4 km long quasi-linear array which crossed the entire fault zone and consisted of 132 nodes. The node spacing was ~15 m within ~500 m of the Mission Creek and Banning surface traces, and ~50 m elsewhere. Two gridded sub-arrays around the traces of the Mission Creek Fault and Banning Fault segments were also installed, but data from these sub-arrays were not used in this study. The instruments were deployed in March 2020, with data collection for the both the quasi-linear and gridded arrays spanning approximately one month. During this period, the array registered clear seismic waves from numerous local earthquakes and eight regional and teleseismic events. Additional details about the array deployment may be found in Share, Qiu, et al. (2022). The location of the array deployment is roughly coincident with Line 5 (stations 502790–503240) from the Salton Sea Imaging Project (SSIP) (Rose et al., 2013), where larger-aperture arrays for seismic reflection and potential-field modeling have been deployed (Fuis et al., 2017; Persaud et al., 2016; Share, Peacock, et al., 2022). This location is approximately 28 km northwest from the northernmost location where InSAR data revealed surface creep large enough for inverse modeling (Figures 1 and 3).

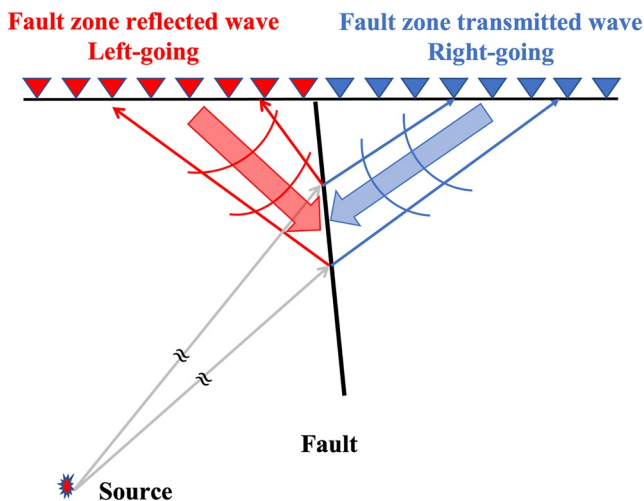### 3.2. Fault Zone Reflected and Transmitted Waves

Active fault mapping (Jennings & Bryant, 2010; USGS, 2020) and regional seismic velocity models (Share & Ben-Zion, 2016) based on different measurements and techniques indicate that the active SSAF separates two crustal blocks. These blocks are modeled with distinct seismic velocities (Share & Ben-Zion, 2016). The polarity of the velocity contrast is reversed across the bend in the San Gorgonio Pass (Share & Ben-Zion, 2016; Zigone et al., 2015). Seismic waves passing through the SSAF could refract along the velocity contrast (i.e., bimaterial interface) and produce fault zone head waves, reflect from the interface and produce fault zone reflected waves (FZRWs), or be transmitted through the interface (Figure 9; Ben-Zion & Aki, 1990). Here, we present imaging results based on reverse time migration (RTM; e.g., Yilmaz, 2001) of fault zone reflected and transmitted waves recorded by the linear array.

Figure 10a shows ~2-s-long P waveforms associated with an earthquake in the San Jacinto fault zone (star in Figure 8a) as recorded by the array. Clear and coherent arrivals after the direct P waves (outlined by the red boxes in Figure 8d) are observed. These secondary arrivals merge with the direct P wave at stations close to the
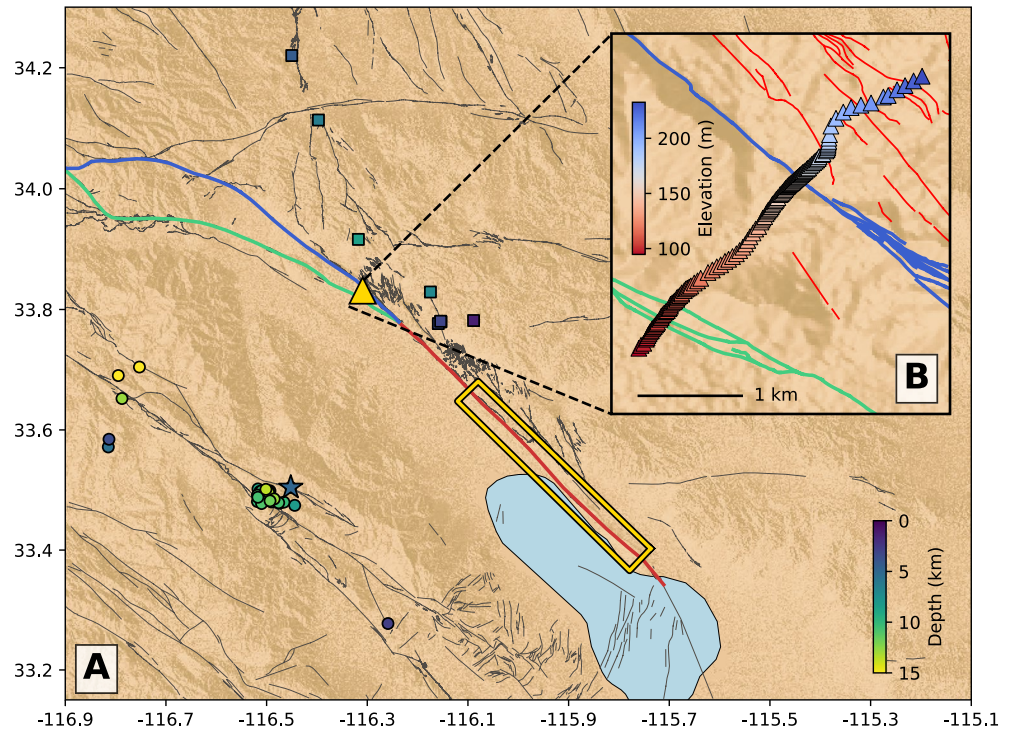
Figure 8. (a) Distribution of events with fault zone reflected waves (FZRWs) used in the reverse time migration (RTM) analysis overlain on shaded-relief topography. The yellow triangle shows the location of the seismic array near Thousand Palms. The yellow box indicates the portion of the SSAF where geodetic inversions were performed. Squares indicate events used to image the Banning Fault (BF) while circles indicate events used to image the Mission Creek Fault (MCF). The star corresponds to the example event shown in Figure 10. Events are colored by focal depth. Dark gray lines indicate Quaternary fault surface traces (USGS, 2020). (b) Configuration of the linear array used in FZRW detection and RTM. The color of each station (triangles) corresponds to its elevation.

Figure 9. Schematic diagram of the reverse time migration of fault zone reflected and transmitted wavefields. An incident seismic wavefield (gray arrows) from a local or teleseismic source interacts with a bimaterial fault zone (black line), producing reflected (thin red arrows and curves) and transmitted (thin blue arrows and curves) wavefields on either side of the fault zone. Wavefields measured by receivers at the surface (triangles) are back-propagated (thick red and blue arrows) through reverse-time migration to image the location and shape of the fault.

fault surface traces (i.e., green and blue dashed lines) and show a move-out opposite to the direct P wave (i.e., the waves arrive earlier at stations that are further away). These observations indicate that the detected secondary phases are reflected P waves from the impedance contrast interfaces of the Banning Fault and Mission Creek Fault. Such FZRWs are observed for more than 30 events indicated in Figure 8a. Arrival times of the FZRWs are sensitive to the geometry of the fault interface and are used to infer the dips of the Banning Fault and Mission Creek Fault beneath the linear array (Figure 9).

We image the subsurface geometry of the major reflection interfaces with a novel RTM technique (Qiu et al., 2023). A traditional migration can be summarized by the following four steps: (a) back-propagate the recorded FZRWs into the subsurface structure; (b) forward simulate the wavefield of the direct wave using the source mechanism and event location; (c) correlate the forward and backward wavefields generated at each time step in the previous two steps; (d) integrate the wavefield correlation over time to obtain the migration image. However, traditional RTM methods require knowledge of the source (i.e., locations, time function, and focal mechanism) and an accurate velocity model of the structure between the source and receivers, which are often poorly constrained. Here, we use the fact that the cross-fault linear array records not only FZRWs but also transmitted waves on the other side of the fault interface. The reflected and transmitted waves are generated at the same time and separated at the same location on the fault interface (Figure 9).
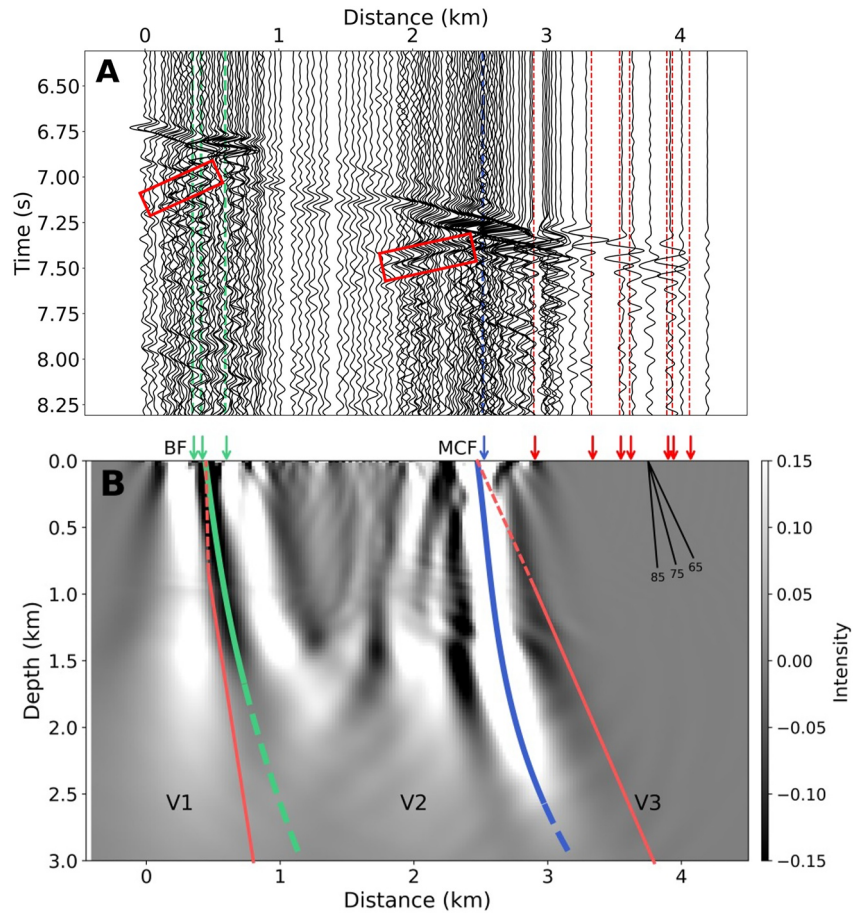
Figure 10. (a) Vertical component P waveforms corresponding to the example event shown in Figure 8. Dashed lines represent surface traces of the Banning Fault (BF) (green), Mission Creek Fault (MCF) (blue), and other subsidiary mapped fractures (red) as they intersect with the array (Figure 8; USGS, 2020). Red boxes outline fault zone reflected waves (FZRWs). (b) Reverse time migration (RTM) image stacked over all FZRW generating events. Green and blue curves denote the interpreted fault geometry of BF and MCF in the top 3 km. Solid red lines show the BF and MCF geometries from Langenheim and Fuis's (2022) potential field modeling, with dashed red lines connecting the modeled geometries to their corresponding surface traces. Based on the polarity of FZRWs, $V1 < V2 < V3$. Reference interfaces with dip angles of 65, 75, and 85° are shown at the top right. Arrows indicate mapped surface fault traces corresponding to those shown in (a).

Thus, we use a new RTM scheme by correlating backward wavefields of the reflected and transmitted waves to image the fault interface. The imaging condition is the correlation (i.e., zero-lag cross-correlation) of fault zone reflected and transmitted wavefields:

$$I(x) = \int U_r(x,t)U_t(x,t)dt \tag{5}$$

where $U_r(x, t)$ and $U_t(x, t)$ are back-propagated fault zone reflected and transmitted wavefields, respectively. Separating fault zone reflected and transmitted wavefields from the full back-propagated wavefield is not a trivial task. We employ the wavefield separation imaging condition (Fei et al., 2015), which was originally developed for isolating the cross-correlation between the down-going source $U_{down}(x, t)$ and up-going receiver $U_{up}(x, t)$ wavefields for traditional reverse time migration methods:

$$I(x) = \int U_{down}(x,t)U_{up}(x,t)dt. \tag{6}$$

In our case, we replace the notation of up- and down-going to left- and right-going, $U_{left}(x, t)$ and $U_{right}(x, t)$, as the reflected and transmitted waves are traveling at opposite directions in the horizontal direction (Figure 9). To

separate the left- and right-going wavefield from the full back-propagated wavefield $U_{full}(x, t)$, we use the Hilbert transform of the wavefields and the final imaging condition is given by:

$$I(x) = \int \left[U_{full}(x,t)U_{full}(x,t) - H_x(U_{full})H_x(U_{full}) \right] dt, \tag{7}$$

where H_x is Hilbert transform in the horizontal direction.

Compared to the traditional RTM, the principal difference and advantage of the new method is that no source field extrapolated into the subsurface is needed. This eliminates the dependence of the imaging result on the accuracy of the source information. Moreover, we only need to propagate surface recordings back to the fault interface, so the imaging result is only sensitive to structures close to the target fault interface.

3.3. Results

Figure 8b shows the imaged subsurface structures of the Banning Fault and Mission Creek Fault based on the new RTM, using the CVM-S4.26 (Lee et al., 2014) as a reference velocity model and fault zone reflected and transmitted waves from the >30 events marked in Figure 8a. The fault interfaces are highlighted by large absolute values of the image intensity with the sign (indicated by black or white color) controlled by the polarity of the reflected wave. The inferred fault interfaces (green and blue curves in Figure 10b) suggest that both the Mission Creek Fault and Banning Fault dip to the northeast in the top 3 km, with increasing dip angle with depth.

The surface location of the inferred Mission Creek Fault interface agrees well with the mapped surface trace and, similarly, the anomaly associated with the Banning Fault is centered amongst associated mapped surface fractures (Figure 8b). We observe that the Mission Creek and Banning Fault anomalies have opposite signs. Since the Banning Fault is imaged with events northeast of the array and the Mission Creek Fault is imaged with events southwest of the array (Figure 8a), the polarity contrast reflects lateral increases in seismic velocities from northeast to southwest across the faults (Figure 10b).

The feature associated with the Mission Creek Fault is both brighter and wider than that of the Banning Fault, indicating that the Mission Creek Fault has a more developed fault damage zone. This observation is consistent with a recent study by Blisniuk et al. (2021), whose updated long-term slip rates on the Mission Creek Fault and Banning Fault near Thousand Palms Oasis suggest the Mission Creek Fault as the main active strand of the SSAF at this location. A broader and more pronounced velocity anomaly near the Mission Creek Fault compared to that near the Banning Fault (Figure 8a), as well as the continuation of shallow creep onto the Mission Creek Fault strand (Figure 3) lend support to the interpretation of Blisniuk et al. (2021). Although earthquakes recorded during the temporary deployment are insufficient to constrain the fault geometry below 3 km using migration, a continued dip of the SSAF at depths >10 km is suggested by head waves recorded at stations of the regional network (Share & Ben-Zion, 2016).

The observed reflectivity pattern in the RTM imaging is in contrast to several previous seismic imaging studies (Fuis et al., 2017; Persaud, 2016). Initial pre-stack line migration results along Line 5 of the SSIP, co-located with our temporary array, identify stronger reflectors associated with the Banning Fault than with the Mission Creek Fault (Persaud, 2016). A similar pattern is observed in reverse-moveout reflections along Line 6 of the SSIP, located about 25 km northeast and along-strike of Line 5 (Fuis et al., 2017). These variations in observed reflectors may arise from differences in imaging techniques, as well as the fact that our nodal array has much finer near-fault resolution in comparison with the SSIP arrays. Seismic nodes along SSIP Line 5 have ~110 m spacing, while our quasi-linear array is nearly an order of magnitude finer (~15 m spacing) within ~500 m of the Mission Creek and Banning fault traces. This allows us to better resolve features in the shallow subsurface. The broader aperture (~38 km) of the SSIP enables imaging of deeper parts of the crust (Fuis et al., 2017; Persaud et al., 2016), while our data provide coverage in the top ~3 km. Furthermore, slip partitioning between the major segments of the SAF system remains ambiguous in the vicinity of SSIP Line 6 and further northwest (cf. Blisniuk et al., 2021), so it would not be unexpected for fault zone structure and reflectivity to vary along strike.

In addition to CVM-S4.26, we explored other reference regional velocity models for the RTM, including CVM-H15.1 (Shaw et al., 2015) and that of Ajala et al. (2019), with the latter providing higher-resolution P-wave velocities V_P in the Salton Trough. We found minimal differences in the resulting RTM images, which is not surprising due to the nature of the RTM technique proposed in this study. Since we use reflected and transmitted

waves, surface recordings are only propagated back to the fault interface. The migration result is subsequently only sensitive to structures between the reflection/transmission points and surface stations (i.e., local structures in the top few kilometers of the crust). In traditional RTM applications, the wavefields are back-propagated from both the surface stations and the source location, requiring an accurate velocity model which encompasses both the source and all receiver stations. With our technique, input velocity models which are similar to the first order will not significantly affect the resultant RTM images. While the V_P model of Ajala et al. (2019) is higher-resolution than the CVM models, we found that CVM-S4.26 produced sharper RTM images. This may be due to differences between the actual velocities provided by the models in the vicinity of the array, rather than their resolutions.

4. Discussion

We present seismic and geodetic observations which render independent but complementary images of the shallow subsurface architecture of the SSAF. Space geodetic data constrain the orientation of the actively slipping interface along a ~40 km portion of the SSAF, while seismic data illuminate the fault damage zones associated with the Mission Creek and Banning Fault segments to the north of the shallowly creeping section. The overall agreement between the two data sets provides good evidence that the entire straight section of the SSAF between Thousand Palms Oasis and Bombay Beach, California is dipping to the northeast in at least the top 2–3 km of the Earth's crust. To investigate the connection of the shallow, creeping interface to the deeper extension of the fault through the mid-to-lower crust, we compare our geodetic inversion results to precisely located seismicity (Ross et al., 2019) and inferred fault geometries obtained from previous studies.

Seismicity along the Coachella Valley segment of the SSAF is characterized by an apparent offset from the main fault trace (Figures 1 and 5; Lin et al., 2007). To facilitate comparison between the near-surface fault geometry suggested by inversions of geodetic data and local seismicity, we project the range of plausible dip angles obtained from the 1σ uncertainties obtained from our Bayesian uncertainty estimates to seismogenic depths (gray lines, Figures 5d–5f). We find that this simple comparison yields good consistency between the modeled shallow geometry and seismicity (Figures 5d–5f and 7) and, in principle, these data sets can be explained by a quasi-planar primary SSAF with dip of ~60–80°. A challenge in making this interpretation is that some seismicity may be accommodated by subsidiary faults northeast of the main SSAF trace (Figures 1, 3, and 5) that been interpreted to comprise a wedge-like flower structure which tapers toward the primary SSAF (Bergh et al., 2019; Fuis et al., 2017).

Seismicity within 3 km of our Box Canyon profile ($y = 30$ km) is mostly segregated into two clusters, both of which reflect northeast-dipping structures (Figures 5d and 7). At this location, our inversions suggest a dip angle of $\theta = 70 \pm 11°$ with slip occurring to depths of 2.0 ± 0.6 km (black line, Figure 5d). The mean modeled dip of 70° coincides better with the deeper cluster at Box Canyon, although the second is within estimated dip uncertainties (Figure 5d). However, we note that our shallow fault models at Box Canyon do not preclude a non-planar fault geometry. There is good agreement with the shallow SSAF geometry obtained from seismic reflection analysis and potential field modeling of Fuis et al. (2017), whose modeled SSAF dips at ~75–80° near the surface, but becomes more gentle below ~6 km in a concave-up manner similar a listric fault (dark gray lines, Figure 5d). The SSAF geometry of Fuis et al. (2017) is slightly shallower that the deeper cluster; a slightly steeper rendition of their geometry would be in better agreement.

East of the SSAF, between Painted Canyon and Box Canyon (Figure 3), Fuis et al. (2017) identify both southwest-dipping and steeply-northeast dipping reflectors in the top 4 km of the crust. They attribute shallower seismicity to an inferred deep segment of the Platform Fault (dashed blue line, Figure 5d), as set of steep reflectors at 3–4 km depth lie directly below the surface trace of the Platform Fault. Similar packages of reflectors are identified at 1.5–4 km are interpreted as the deeper extent of the Painted Canyon Fault. However, shallow southwest-dipping reflectors over 1–1.5 km depth also coincide with the surface traces of the Skeleton Canyon and Painted Canyon Faults, which is in agreement with detailed geologic mapping and reconstruction in the Mecca Hills (Bergh et al., 2019). Thus, we suggest it is unlikely that the Painted Canyon Fault or Skeleton Canyon Fault contribute to either northeast dipping cluster of seismicity at depths >5 km. We also note that agreement with our geodetic modeling results is slightly better with the fault geometry which best fits potential field data sets, which indicates a gentler dip in the top ~6 km of the crust (Fuis et al., 2017). While comparison between our results and those of Fuis et al. (2017) is useful, some differences in

the resolved fault geometry stemming from the aperture of the profiles used, as well as the orientation of the profiles (there is a ~15° difference in azimuth between our InSAR profile at Box Canyon and SSIP Line 4) are not surprising. Importantly, all available data sets indicate that the SSAF dips to the northeast in the top 3 km of the crust.

At more southern locations, including at the North Shore and Ferrum sites (Figures 5e and 5f), the shallower, eastern seismicity cluster is more prominent (Figures 5 and 7). It is possible that this seismicity may be attributed to the Platform Fault (Figures 5e and 5f) or the Hidden Spring Fault at the latitude of Ferrum (Figure 5f), if their geometries are also northeast dipping (Fuis et al., 2017). However, the shallower cluster is also compatible with a relatively simple quasi-planar SSAF with a northeast dip of ~55–60°. The events below the dominant clusters would be in-line with a more steeply dipping SSAF if the Platform or Hidden Spring Fault is indeed seismically active at depths 5–12 km. In absence of additional constraints on the shallow geometries of the SSAF and other subsidiary northeastern faults, it is difficult to determine with certainty which structures seismicity is associated with southeast of Box Canyon.

In summary, while there is ambiguity regarding which structures host most of the seismicity in the vicinity of the Coachella section of the SSAF, our shallow fault models are compatible with both quasi-planar and concave-up geometries which connect with clusters of seismicity at depth. Locations where this is not the case coincide with spurious shallow dip angles (Figure 7), which we do not interpret to be robust due to low signal-to-noise ratio and data gaps in the InSAR velocity field (Figure 3c). In addition to seismicity locations, local focal mechanisms (Hutton et al., 2010) from M_w 2+ events that have a strike similar to the SSAF exhibit dip angles ranging from 45 to 70° (Figure S5 in Supporting Information S1). Lastly, we note we find no models or earthquake locations which suggest a vertical SSAF — throughout the crust or its uppermost <5 km.

Good alignment of the shallow creeping interface with the seismically active structures at depth suggests that much of the fault is quasi-planar, with an overall dip angle of $\theta \approx 60$–70°. However, while our results do not require strong non-planarity in regions where the fault-parallel velocity field is robust, our geodetic modeling results do not preclude some down-dip variations in the fault dip angle (i.e., Fuis et al., 2017) given our depth sensitivity and dip angle uncertainty estimates. Importantly, all SSAF geometries with northeast dip throughout the crust—with morphologies ranging from quasi-planar to concave-up—are consistent with fault dip angles derived from inversions of the long-wavelength interseismic deformation data that are primarily sensitive to the fault location at the bottom of the seismogenic zone (Fialko, 2006; Lindsey & Fialko, 2013), as well as sharp contrasts at ~10 km depth in seismic velocities obtained from double-difference tomography (Share et al., 2019). Such an agreement implies that the shallow creep and the seismically active structures below 5 km depth are part of the same localized fault zone.

In addition, crustal tilting of the central Salton block, between the SJF and SSAF, provides additional support for a northeast-dipping SSAF in the Coachella Valley (Dorsey & Langenheim, 2015). The most plausible mechanism for tilting is transpression across a northeast dipping SSAF, where the combination of oblique convergence and fault dip induces a vertical load that tilts the central Salton block to the northeast. Jänecke et al. (2018) note that the Eastern Shoreline Fault is the westernmost structure bounding the central Salton block at the surface, located 1–3 km southwest and parallel to the primary SSAF surface trace along its southernmost ~30 km. They interpret that the Eastern Shoreline Fault is a subsidiary fault within a broader northeast-dipping flower structure associated with the main SSAF. In this case, the Eastern Shoreline Fault connects with the creeping primary surface expression of the SSAF at several kilometers depth, which is consistent with reverse-moveout reflections detected near the northern end of the Salton Sea (SSIP Line 4, Fuis et al., 2017). These interpretations are consistent with the steep-to-moderate northeast dip (~70° ± 10° through the Mecca Hills) we obtain from inversions of displacements due to shallow creep (Figure 7).

Topographic asymmetry in the southern Santa Rosa Mountains (and lack thereof further north in the San Jacinto Mountains) indicates the northwestward extent of tilting between the SJF and SSAF fault zones (Dorsey & Langenheim, 2015). While the combination of diminishing creep signal and poor coverage of InSAR measurements limits our ability to resolve the shallow SSAF geometry north of the Mecca Hills with space geodesy, our RTM imaging results near Thousand Palms Oasis indicate steeper northeast dips (75–85°; Figure 8e). This, in conjunction with the inferred decrease or absence of crustal tilting, may reflect wholesale steepening at the bifurcation into the Mission Creek Fault and Banning Fault relative to the section of the SSAF south of the Mecca Hills. Co-located magnetotelluric imaging (Share, Peacock, et al., 2022), furthermore clearly indicates a northeast dipping conductor in the shallow crust where the model resolution is greatest.

In summary, we find evidence along the entire Coachella Valley section of the active SSAF that the fault is dipping to the northeast in the uppermost crust with a dip angle of 60–80° (Figures 5, 7, and 10). Since shallow creep occurs along the primary fault trace that has accommodated long-term slip, the shallow geometries we model likely connect to the deeper locked portion of the fault, where maximum coseismic slip is anticipated. Given the general agreement of our inferred shallow northeast dipping geometry with an abundance of ancillary evidence for a moderately-dipping SSAF in the mid-to-lower crust, we suggest that the entire Coachella Valley SSAF dips significantly to the northeast. Our models of the shallow fault geometry are consistent with a moderately-dipping and quasi-planar SSAF (Figures 5d–5f), and/or a more gently dipping SSAF which slightly steepens up-dip in a listric fashion (Figures 5d and 10) depending on the along-fault location. The overall northeast dipping geometry is supported by evidence of regional tectonics (Dorsey & Langenheim, 2015; Langenheim & Fuis, 2022) and mechanical modeling of the long-term fault slip that predicts patterns of uplift and subsidence across the SSAF (Fattaruso et al., 2014). An alternative interpretation would involve a highly non-planar fault which has a northeast dip in the top several kilometers but curves southwest to a vertical attitude at greater depths, devoid of any seismicity. This model has been suggested on the basis of electromagnetic modeling near Thousand Palms Oasis/SSIP Line 5 (Share, Peacock, et al., 2022), although presently no additional evidence lends itself to support this scenario.

The non-vertical orientation of the predominantly strike-slip SSAF has several important implications. It significantly affects estimates of the secular fault slip rate that otherwise appear too high compared to the long-term geologic slip rates (Lindsey & Fialko, 2013). The dip angles determined in this study confirms the results of Lindsey and Fialko (2013), who documented a northeast dip of the fault and indicated no systematic difference between geologic slip rates (Behr et al., 2010; Van Der Woerd et al., 2006) applicable to timescales of 10^5–10^6 years and geodetic rates applicable to the last few decades.

Recent work has also showed that a non-vertical fault dip affects the fault sensitivity to hydrologic loads (Hill et al., 2023), the dynamics of earthquake ruptures, including the radiation pattern, the likelihood of rupture propagation through the San Gorgonio bend at the north, and, ultimately, the size of major earthquakes on the SSAF system (Douilly et al., 2020; Lozos, 2021; Padilla et al., 2022). Numerical simulations indicate that the intensity of ground shaking for a dipping versus vertical fault may differ by up to a factor of two within a few tens of kilometers from the earthquake rupture (Fuis et al., 2017). A well-constrained fault geometry is therefore essential for accurate predictions of ground motion in densely populated areas in Southern California (Böse et al., 2014; Roten et al., 2014).

The revised fault geometry also provides a useful input for studies of the state of stress at seismogenic depths (Fialko, 2021; Fialko et al., 2005), the evolution and structure of fault damage zones (Lindsey, Fialko, et al., 2014), and their effects on the long-term earthquake cycle behavior (Thakur et al., 2020). An unusual aspect of a non-vertical strike-slip fault is that it increases the coseismic slip area, the seismic moment, and the total amount of work done against friction compared to the canonical vertical orientation. If a minimum work principle applies to mature fault systems (Michael, 1990), one can estimate the effective strength of a dipping fault to be less than that of a vertical fault by at least a factor of $\sin \theta$. All other conditions being equal, it means that a dipping fault has to be either statically or dynamically weaker than a better oriented potential vertical fault. One possible explanation is inheritance of a pre-existing tectonic fabric (Schulte-Pelkum et al., 2020). There is growing evidence that the non-vertical strike-slip faults may be more common than previously thought (Árnadóttir & Segall, 1994; Avouac et al., 2014; Funning et al., 2007; Tong et al., 2010). The methods and results presented in this study may help identify such faults and constrain their configuration at depth before they generate large earthquakes.

5. Conclusions

The geometry of the Coachella Valley section of the active Southern San Andreas Fault (SSAF) has long been debated, in part due to a paucity of geophysical observations in the shallow subsurface. In this study, we incorporate insights from RTM analyses of FZRWs, the spatial distribution of earthquake locations, and inverse modeling of shallow fault creep that provide a consistent view of the shallow structure of the SSAF and its connection to the deeper seismogenic fault zone. Along most of the SSAF in the Coachella Valley, both geodetic and seismic observations are best explained by a northeast dip of the fault at 60–70° in the upper few kilometers of the crust. At the bifurcation of the SSAF into the Mission Creek Fault and Banning Fault branches near Thousand Palms,

both branches are also dipping to the northeast with a dip angle that decreases from ~80° near the surface to <70° below a depth of 2 km. We suggest that the shallow structure highlighted by our new observations is part of the same throughgoing primary fault interface which generates destructive earthquakes. When considering our models of the shallow fault geometry in the context of other geological and geophysical studies, we suggest that the most straightforward interpretation is that the SSAF has a component of northeast dip throughout the seismogenic zone along much of the Coachella Valley section of the SSAF.

Appendix A: Bayesian Inversion Methodology

Since our forward model describing the relationship between the fault geometry and surface deformation (Equation 2) is non-linear, we use a Bayesian inverse approach to develop a suite of plausible models given the level of noise present in our data. From the resulting collection of models, we can compute statistics to analyze the likelihood of various combinations of fault geometry and slip rate. First, we consider Bayes rule,

$$p(\mathbf{m}|\mathbf{d}) = \frac{p(\mathbf{d}|\mathbf{m})p(\mathbf{m})}{p(\mathbf{d})} \tag{A1}$$

where the posterior distribution $p(\mathbf{m}|\mathbf{d})$ describes the probability of model $\mathbf{m}$ given data $\mathbf{d}$, the likelihood distribution $p(\mathbf{d}|\mathbf{m})$ describes the probability of obtaining data $\mathbf{d}$ for a given model $\mathbf{m}$, the prior distribution $p(\mathbf{m})$ containing a priori information about $\mathbf{m}$, and $p(\mathbf{d})$ is the model evidence. The model evidence $p(\mathbf{d})$ is constant for all possible $\mathbf{m}$, and thus may be neglected during Bayesian sampling. Bayes rule (A1) is then reduced to,

$$p(\mathbf{m}|\mathbf{d}) \propto p(\mathbf{d}|\mathbf{m})p(\mathbf{m}), \tag{A2}$$

which can be used to draw samples in a Markov chain Monte Carlo (MCMC) framework. The likelihood $p(\mathbf{d}|\mathbf{m})$ is formed on the assumption that the data-model residuals $\mathbf{d} - \mathbf{v}(\mathbf{m})$ should be Gaussian with covariance matrix $\mathbf{C}$.

$$p(\mathbf{d}|\mathbf{m}) \propto \exp\left(-\frac{1}{2}(\mathbf{d} - \mathbf{v}(\mathbf{m}))^T \mathbf{C}^{-1}(\mathbf{d} - \mathbf{v}(\mathbf{m}))\right) \tag{A3}$$

While InSAR data have spatial covariances (Lohman & Simons, 2005), we only consider estimates of data errors $\boldsymbol{\sigma}$ obtained during our down-sampling procedure and construct a diagonal data covariance matrix $\boldsymbol{\Sigma}$, which may be inverted in an element-wise fashion. To form the inverse of the likelihood covariance matrix $\mathbf{C}^{-1}$, we include a diagonal matrix $\mathbf{B}$, composed of the along-strike smoothing weights b, so that $\mathbf{C}^{-1} = \boldsymbol{\Sigma}^{-1}\mathbf{B}$. The formation of $\boldsymbol{\Sigma}$ and $\mathbf{B}$ is discussed in further detail in Section 2.4. Since we use a uniform prior distribution, $p(\mathbf{m})$ a constant over all $\mathbf{m}$ and can be dropped from Equation 6 due to proportionality and implemented as bounds on the proposed $\mathbf{m}$ states. Thus, the final form of the posterior $p(\mathbf{m}|\mathbf{d})$ supplied to the Bayesian sampling algorithm is equivalent to (Equation A3).

We draw samples from (Equation A3) using the *emcee* implementation of an affine invariant Markov chain Monte Carlo (MCMC) ensemble sampler (Foreman-Mackey et al., 2013; Goodman & Weare, 2010). We utilize this sampling algorithm due to its efficiency for low-dimensional problems where strong correlations and/or anisotropies may exist in the parameters' probability space (Goodman & Weare, 2010). For each 2D fault inversion, we run an ensemble with 10^2 members (i.e., random walks) for 10^5 steps, giving 10^7 initial samples from the posterior distribution. To improve the independence of our samples, we compute the integrated auto-correlation time τ of each model parameter's Markov chain using the method described by Sokal (1997) as implemented in the *emcee* package (Foreman-Mackey et al., 2013). We discard the first $2\tau_{\max}$ samples and decimate each chain by a factor of $1/2\tau_{\min}$. Typical values of τ range between 40 and 70, resulting in 4–5×10^5 effective samples per Bayesian inversion. All posterior distribution statistics are computed using only the effective samples derived from autocorrelation analysis.

Data Availability Statement

Raw Sentinel-1 data used in generating InSAR time series and velocity maps are openly available from Alaska Satellite Facility via https://search.asf.alaska.edu (ASF, 2022). Original GNSS positions used to generate secular tectonic velocities can be freely downloaded from the Scripps Orbit and Permanent Array Center via http://sopac-csrc.ucsd.edu/index.php/data-download (SOPAC, 2022) and the Eartscope Geodetic Facility for the Advancement of Geoscience Data Center via https://www.unavco.org/data/gps-gnss/gps-gnss.html (EarthScope, 2022).

Post-processed InSAR and GNSS velocity fields used in geodetic inversions can be accessed from Zenodo via https://zenodo.org/record/7719223 (Vavra & Fialko, 2023). The nodal array locations and waveform data can be accessed from the Incorporated Research Institutions for Seismology Data Management Center via https://www.fdsn.org/networks/detail/YA_2020/ (Vernon et al., 2020). Earthquake locations and focal mechanisms used in assessing fault geometry, as well as metadata for local and teleseismic events used in the array analysis are openly accessible from the Southern California Earthquake Center via https://scedc.caltech.edu/data (SCEDC, 2013).

References

Ajala, R., Persaud, P., Stock, J. M., Fuis, G. S., Hole, J. A., Goldman, M., & Scheirer, D. (2019). Three-dimensional basin and fault structure from a detailed seismic velocity model of Coachella Valley, southern California. *Journal of Geophysical Research: Solid Earth*, *124*(5), 4728–4750. https://doi.org/10.1029/2018JB016260

Allen, C. R., Wyss, M., Brune, J. N., Grantz, A., & Wallace, R. E. (1972). *Displacements on the Imperial, Superstition Hills, and San Andreas faults triggered by the Borrego Mountain earthquake*. [Geological Survey Professional Paper. No.787].

Anderson, E. M. (1951). *The dynamics of faulting and dike formation with application to Britain* (p. 206). Oliver and Boyd.

Árnadóttir, T., & Segall, P. (1994). The 1989 Loma Prieta earthquake imaged from inversion of geodetic data. *Journal of Geophysical Research*, *99*(B11), 21835–21855. https://doi.org/10.1029/94jb01256

ASF. (2022). European Space Agency Copernicus Sentinel data [Dataset]. Alaska Satellite Facility Distributed Active Archive Center. Retrieved from https://search.asf.alaska.edu/

Avouac, J.-P., Ayoub, F., Wei, S., Ampuero, J.-P., Meng, L., Leprince, S., et al. (2014). The 2013, M_w 7.7 Balochistan earthquake, energetic strike-slip reactivation of a thrust fault. *Earth and Planetary Science Letters*, *391*, 128–134. https://doi.org/10.1016/j.epsl.2014.01.036

Bawden, G. W., Thatcher, W., Stein, R. S., Hudnut, K. W., & Peltzer, G. (2001). Tectonic contraction across Los Angeles after removal of ground-water pumping effects. *Nature*, *412*(6849), 812–815. https://doi.org/10.1038/35090558

Behr, W. M., Rood, D. H., Fletcher, K. E., Guzman, N., Finkel, R., Hanks, T. C., et al. (2010). Uncertainties in slip-rate estimates for the Mission Creek strand of the southern San Andreas fault at Biskra Palms Oasis, southern California. *Geological Society of America Bulletin*, *122*(9–10), 1360–1377. https://doi.org/10.1130/B30020.1

Bennett, R. A., Rodi, W., & Reilinger, R. E. (1996). Global positioning system constraints on fault slip rates in southern California and northern Baja, Mexico. *Journal of Geophysical Research*, *101*(B10), 21943–21960. https://doi.org/10.1029/96jb02488

Ben-Zion, Y., & Aki, K. (1990). Seismic radiation from an SH line source in a laterally heterogeneous planar fault zone. *Bulletin of the Seismological Society of America*, *80*(4), 971–994. https://doi.org/10.1785/bssa0800040971

Bergh, S. G., Sylvester, A. G., Damte, A., & Indrevær, K. (2019). Polyphase kinematic history of transpression along the Mecca Hills segment of the San Andreas Fault, southern California. *Geosphere*, *15*(3), 901–934. https://doi.org/10.1130/ges02027.1

Bilham, R., & Williams, P. (1985). Sawtooth segmentation and deformation processes on the southern San Andreas fault, California. *Geophysical Research Letters*, *12*(9), 557–560. https://doi.org/10.1029/gl012i009p00557

Blisniuk, K., Scharer, K., Sharp, W. D., Burgmann, R., Amos, C., & Rymer, M. (2021). A revised position for the primary strand of the Pleistocene-Holocene San Andreas fault in southern California. *Science Advances*, *7*(13), 5691–5715. https://doi.org/10.1126/sciadv.aaz5691

Bock, Y., Kedar, S., Moore, A. W., Fang, P., Geng, J., Liu, Z., et al. (2017). Twenty-two years of combined GPS products for geophysical applications and a decade of seismogeodesy. In *International symposium on geodesy for earthquake and natural hazards (GENAH)* (pp. 49–54).

Böse, M., Graves, R. W., Gill, D., Callaghan, S., & Maechling, P. J. (2014). CyberShake-derived ground-motion prediction models for the Los Angeles region with application to earthquake early warning. *Geophysical Journal International*, *198*(3), 1438–1457. https://doi.org/10.1093/gji/ggu198

Bürgmann, R. (1991). Transpression along the southern San Andreas fault, Durmid Hill, California. *Tectonics*, *10*(6), 1152–1163. https://doi.org/10.1029/91tc01443

Chaussard, E., Bürgmann, R., Shirzaei, M., Fielding, E. J., & Baker, B. (2014). Predictability of hydraulic head changes and characterization of aquifer-system and fault properties from InSAR-derived ground deformation. *Journal of Geophysical Research: Solid Earth*, *119*(8), 6572–6590. https://doi.org/10.1002/2014jb011266

Dorsey, R. J., & Langenheim, V. E. (2015). Crustal-scale tilting of the central Salton block, southern California. *Geosphere*, *11*(5), 1365–1383. https://doi.org/10.1130/ges01167.1

Douilly, R., Oglesby, D. D., Cooke, M. L., & Hatch, J. L. (2020). Dynamic models of earthquake rupture along branch faults of the eastern San Gorgonio pass region in California using complex fault structure. *Geosphere*, *16*(2), 474–489. https://doi.org/10.1130/ges02192.1

EarthScope (2022). Global navigation satellite system position solutions [Dataset]. Geodetic Facility for the Advancement of Geoscience. Retrieved from https://www.unavco.org/data/gps-gnss/gps-gnss.html

Farr, T. G., Rosen, P. A., Caro, E., Crippen, R., Duren, R., Hensley, S., et al. (2007). The shuttle radar topography mission. *Reviews of Geophysics*, *45*(2), RG2004. https://doi.org/10.1029/2005rg000183

Fattaruso, L. A., Cooke, M. L., & Dorsey, R. J. (2014). Sensitivity of uplift patterns to dip of the San Andreas fault in the Coachella Valley, California. *Geosphere*, *10*(6), 1235–1246. https://doi.org/10.1130/ges01050.1

Fei, T. W., Luo, Y., Yang, J., Liu, H., & Qin, F. (2015). Removing false images in reverse time migration: The concept of de-primary. *Geophysics*, *80*(6), S237–S244. https://doi.org/10.1190/geo2015-0289.1

Ferretti, A., Prati, C., & Rocca, F. (2001). Permanent scatterers in SAR interferometry. *IEEE Transactions on Geoscience and Remote Sensing*, *39*(1), 8–20. https://doi.org/10.1109/36.898661

Fialko, Y. (2004). Probing the mechanical properties of seismically active crust with space geodesy: Study of the co-seismic deformation due to the 1992 M_w7.3 Landers (southern California) earthquake. *Journal of Geophysical Research*, *109*(B3), B03307. https://doi.org/10.1029/2003JB002756

Fialko, Y. (2006). Interseismic strain accumulation and the earthquake potential on the southern San Andreas fault system. *Nature*, *441*(7096), 968–971. https://doi.org/10.1038/nature04797

Fialko, Y. (2007). Fracture and frictional mechanics - Theory. In G. Schubert (Ed.), *Treatise on geophysics* (Vol. 4, pp. 83–106). Elsevier Ltd.

Fialko, Y. (2021). Estimation of absolute stress in the hypocentral region of the 2019 Ridgecrest, California, earthquakes. *Journal of Geophysical Research: Solid Earth*, *126*(7), e2021JB022000. https://doi.org/10.1029/2021jb022000

Fialko, Y., & Jin, Z. (2021). Simple shear origin of the cross-faults ruptured in the 2019 Ridgecrest earthquake sequence. *Nature Geoscience*, *14*(7), 513–518. https://doi.org/10.1038/s41561-021-00758-5

Fialko, Y., Rivera, L., & Kanamori, H. (2005). Estimate of differential stress in the upper crust from variations in topography and strike along the San Andreas fault. *Geophysical Journal International*, *160*(2), 527–532. https://doi.org/10.1111/j.1365-246x.2004.02511.x

Field, E. H., Arrowsmith, R. J., Biasi, G. P., Bird, P., Dawson, T. E., Felzer, K. R., et al. (2014). Uniform California earthquake rupture forecast, version 3 (UCERF3): The time-independent model. *Bulletin of the Seismological Society of America*, *104*, 1122–1180. https://doi.org/10.1785/0120130164

Foreman-Mackey, D., Hogg, D. W., Lang, D., & Goodman, J. (2013). EMCEE: The MCMC hammer. *Publications of the Astronomical Society of the Pacific*, *125*(925), 306–312. https://doi.org/10.1086/670067

Fuis, G. S., Bauer, K., Goldman, M. R., Ryberg, T., Langenheim, V. E., Scheirer, D. S., et al. (2017). Subsurface geometry of the San Andreas fault in southern California: Results from the Salton Seismic Imaging Project (SSIP) and strong ground motion expectations. *Bulletin of the Seismological Society of America*, *107*(4), 1642–1662. https://doi.org/10.1785/0120160309

Fuis, G. S., Scheirer, D. S., Langenheim, V. E., & Kohler, M. D. (2012). A new perspective on the geometry of the San Andreas fault in southern California and its relationship to lithospheric structure. *Bulletin of the Seismological Society of America*, *102*(1), 236–251. https://doi.org/10.1785/0120110041

Funning, G. J., Parsons, B., & Wright, T. J. (2007). Fault slip in the 1997 Manyi, Tibet earthquake from linear elastic modelling of InSAR displacements. *Geophysical Journal International*, *169*(3), 988–1008. https://doi.org/10.1111/j.1365-246x.2006.03318.x

Goodman, J., & Weare, J. (2010). Ensemble samplers with affine invariance. *Communications in Applied Mathematics and Computational Science*, *5*(1), 65–80. https://doi.org/10.2140/camcos.2010.5.65

Herring, T. A., Melbourne, T. I., Murray, M. H., Floyd, M. A., Szeliga, W. M., King, R. W., et al. (2016). Plate boundary observatory and related networks: GPS data analysis methods and geodetic products. *Reviews of Geophysics*, *54*(4), 759–808. https://doi.org/10.1002/2016rg000529

Hill, R. G., Weingarten, M., Rockwell, T. K., & Fialko, Y. (2023). Major southern San Andreas earthquakes modulated by lake-filling events. *Nature*, *618*(7966), 761–766. https://doi.org/10.1038/s41586-023-06058-9

Hooper, A., Zebker, H., Segall, P., & Kampes, B. (2004). A new method for measuring deformation on volcanoes and other natural terrains using InSAR persistent scatterers. *Geophysical Research Letters*, *31*(23), 19-1–19-4. https://doi.org/10.1029/2002GL016156

Hutton, K., Woessner, J., & Hauksson, E. (2010). Earthquake monitoring in southern California for seventy-seven years (1932-2008). *Bulletin of the Seismological Society of America*, *100*(2), 423–446. https://doi.org/10.1785/0120090130

Jänecke, S. U., Markowski, D. K., Evans, J. P., Persaud, P., & Kenney, M. (2018). Durmid ladder structure and its implications for the nucleation sites of the next $M > 7.5$ earthquake on the San Andreas fault or Brawley seismic zone in southern California. *Lithosphere*, *10*(5), 1–30. https://doi.org/10.1130/l629.1

Jennings, C., & Bryant, W. (2010). Geologic data map no. 6. Fault activity map of California.

Jin, Z., & Fialko, Y. (2020). Finite slip models of the 2019 Ridgecrest earthquake sequence constrained by space geodetic data and aftershock locations. *Bulletin of the Seismological Society of America*, *110*(4), 1660–1679. https://doi.org/10.1785/0120200060

Johnson, H. O., Agnew, D. C., & Wyatt, F. K. (1994). Present-day crustal deformation in southern California. *Journal of Geophysical Research*, *99*(B12), 23951–23974. https://doi.org/10.1029/94jb01902

Jones, L. M., Bernknopf, R., Cox, D., Goltz, J., Hudnut, K., Mileti, D., et al. (2008). The ShakeOut scenario. [USGS Open File Report 2008-1150 and CGS Preliminary Report 25].

Kaneko, Y., Fialko, Y., Sandwell, D., Tong, X., & Furuya, M. (2013). Interseismic deformation and creep along the central section of the North Anatolian fault (Turkey): InSAR observations and implications for rate-and-state friction properties. *Journal of Geophysical Research*, *118*(1), 316–331. https://doi.org/10.1029/2012jb009661

Langenheim, V., & Fuis, G. (2022). Insights into the geometry and evolution of the southern San Andreas fault from geophysical data, southern California. *Geosphere*, *18*(2), 458–475. https://doi.org/10.1130/ges02378.1

Lau, N., Tymofyeyeva, E., & Fialko, Y. (2018). Variations in the long-term uplift rate due to the Altiplano–Puna magma body observed with Sentinel-1 interferometry. *Earth and Planetary Science Letters*, *491*, 43–47. https://doi.org/10.1016/j.epsl.2018.03.026

Lee, E.-J., Chen, P., Jordan, T. H., Maechling, P. B., Denolle, M. A., & Beroza, G. C. (2014). Full-3-D tomography for crustal structure in southern California based on the scattering-integral and the adjoint-wavefield methods. *Journal of Geophysical Research*, *119*(8), 6421–6451. https://doi.org/10.1002/2014jb011346

Lin, G., Shearer, P. M., & Hauksson, E. (2007). Applying a three-dimensional velocity model, waveform cross correlation, and cluster analysis to locate southern California seismicity from 1981 to 2005. *Journal of Geophysical Research*, *112*(B12), B12309. https://doi.org/10.1029/2007JB004986

Lindsey, E. O., & Fialko, Y. (2013). Geodetic slip rates in the southern San Andreas fault system: Effects of elastic heterogeneity and fault geometry. *Journal of Geophysical Research*, *118*(2), 689–697. https://doi.org/10.1029/2012jb009358

Lindsey, E. O., & Fialko, Y. (2016). Geodetic constraints on frictional properties and earthquake hazard in the Imperial Valley, southern California. *Journal of Geophysical Research*, *121*(2), 1097–1113. https://doi.org/10.1002/2015jb012516

Lindsey, E. O., Fialko, Y., Bock, Y., Sandwell, D. T., & Bilham, R. (2014a). Localized and distributed creep along the southern San Andreas fault. *Journal of Geophysical Research*, *119*(10), 7909–7922. https://doi.org/10.1002/2014jb011275

Lindsey, E. O., Sahakian, V. J., Fialko, Y., Bock, Y., Barbot, S., & Rockwell, T. K. (2014b). Interseismic strain localization in the San Jacinto fault zone. *Pure and Applied Geophysics*, *171*(11), 2937–2954. https://doi.org/10.1007/s00024-013-0753-z

Lohman, R. B., & Simons, M. (2005). Some thoughts on the use of InSAR data to constrain models of surface deformation: Noise structure and data downsampling. *Geochemistry, Geophysics, Geosystems*, *6*(1), Q01007. https://doi.org/10.1029/2004gc000841

Lozos, J. C. (2021). The effect of along-strike variation in dip on rupture propagation on strike-slip faults. *Geosphere*, *17*(6), 1616–1630. https://doi.org/10.1130/ges02391.1

Lyons, S., & Sandwell, D. (2003). Fault creep along the southern San Andreas from interferometric synthetic aperture radar, permanent scatterers, and stacking. *Journal of Geophysical Research*, *108*(B1), 2047. https://doi.org/10.1029/2002jb001831

Maghsoudi, Y., Hooper, A. J., Wright, T. J., Lazecky, M., & Ansari, H. (2022). Characterizing and correcting phase biases in short-term, multi-looked interferograms. *Remote Sensing of Environment*, *275*, 113022. https://doi.org/10.1016/j.rse.2022.113022

Manighetti, I., Campillo, M., Bouley, S., & Cotton, F. (2007). Earthquake scaling, fault segmentation, and structural maturity. *Earth and Planetary Science Letters*, *253*(3–4), 429–438. https://doi.org/10.1016/j.epsl.2006.11.004

Mavko, G. M. (1981). Mechanics of motion on major faults. *Annual Review of Earth and Planetary Sciences*, *9*(1), 81–111. https://doi.org/10.1146/annurev.ea.09.050181.000501

Michael, A. (1990). Energy constraints on kinematic models of oblique faulting - Loma-Prieta versus Parkfield-Coalinga. *Geophysical Research Letters*, *9*, 1453–1456. https://doi.org/10.1029/gl017i009p01453

Michaelides, R. J., Zebker, H. A., & Zheng, Y. (2019). An algorithm for estimating and correcting decorrelation phase from InSAR data using closure phase triplets. *IEEE Transactions on Geoscience and Remote Sensing*, *57*(12), 10390–10397. https://doi.org/10.1109/tgrs.2019.2934362

Okada, Y. (1985). Surface deformation due to shear and tensile faults in a half-space. *Bulletin of the Seismological Society of America*, *75*(4), 1135–1154. https://doi.org/10.1785/bssa0750041135

Padilla, A. M., Oskin, M. E., Rockwell, T. K., Delusina, I., & Singleton, D. M. (2022). Joint earthquake ruptures of the San Andreas and San Jacinto faults, California, USA. *Geology*, *50*(4), 387–391. https://doi.org/10.1130/g49415.1

Persaud, P. (2016). Integrated 3-D seismotectonic-velocity model of the salton trough region based on seismicity and explosive shots from the Salton Seismic Imaging Project. *Tech. Rep. No. G15AP00062*.

Persaud, P., Ma, Y., Stock, J. M., Hole, J. A., Fuis, G. S., & Han, L. (2016). Fault zone characteristics and basin complexity in the southern Salton Trough, California. *Geology*, *44*(9), 747–750. https://doi.org/10.1130/g38033.1

Philibosian, B., Fumal, T., & Weldon, R. (2011). San Andreas fault earthquake chronology and Lake Cahuilla history at Coachella, California. *Bulletin of the Seismological Society of America*, *101*(1), 13–38. https://doi.org/10.1785/0120100050

Platt, J. P., & Becker, T. W. (2010). Where is the real transform boundary in California? *Geochemistry, Geophysics, Geosystems*, *11*(6), Q06012. https://doi.org/10.1029/2010gc003060

Qiu, H., Chi, B., & Ben-Zion, Y. (2023). Internal structure of the central Garlock fault zone from Ridgecrest aftershocks recorded by dense linear seismic arrays. *Geophysical Research Letters*, *50*(2), e2022GL101761. https://doi.org/10.1029/2022gl101761

Rizzoli, P., Martone, M., Gonzalez, C., Wecklich, C., Tridon, D. B., Bräutigam, B., et al. (2017). Generation and performance assessment of the global TanDEM-X digital elevation model. *ISPRS Journal of Photogrammetry and Remote Sensing*, *132*, 119–139. https://doi.org/10.1016/j.isprsjprs.2017.08.008

Rose, E. J., Fuis, G. S., Stock, J. M., Hole, J. A., Kell, A. M., Kent, G., et al. (2013). Borehole-explosion and air-gun data acquired in the 2011 Salton Seismic Imaging Project (SSIP), southern California: Description of the survey. USGS Open-File Report 2013-1172.

Ross, Z. E., Trugman, D. T., Hauksson, E., & Shearer, P. M. (2019). Searching for hidden earthquakes in southern California. *Science*, *364*(6442), 767–771. https://doi.org/10.1126/science.aaw6888

Roten, D., Olsen, K., Day, S., Cui, Y., & Fäh, D. (2014). Expected seismic shaking in Los Angeles reduced by San Andreas fault zone plasticity. *Geophysical Research Letters*, *41*(8), 2769–2777. https://doi.org/10.1002/2014gl059411

Sandwell, D., Mellors, R., Tong, X., Wei, M., & Wessel, P. (2011). Open radar interferometry software for mapping surface deformation. *Eos, Transactions, American Geophysical Union*, *92*(28), 234. https://doi.org/10.1029/2011eo280002

SCEDC. (2013). Southern California earthquake data center [Dataset]. Caltech. https://doi.org/10.7909/C3WD3XH1

Schulte-Pelkum, V., Ross, Z. E., Mueller, K., & Ben-Zion, Y. (2020). Tectonic inheritance with dipping faults and deformation fabric in the brittle and ductile southern California crust. *Journal of Geophysical Research*, *125*(8), e2020JB019525. https://doi.org/10.1029/2020jb019525

Segall, P. (2010). *Earthquake and volcano deformation*. Princeton University Press.

Segall, P., & Lisowski, M. (1990). Surface displacements in the 1906 San Francisco and 1989 Loma Prieta earthquakes. *Science*, *250*(4985), 1241–1244. https://doi.org/10.1126/science.250.4985.1241

Share, P.-E., & Ben-Zion, Y. (2016). Bimaterial interfaces in the south San Andreas fault with opposite velocity contrasts NW and SE from San Gorgonio Pass. *Geophysical Research Letters*, *43*(20), 10–680. https://doi.org/10.1002/2016gl070774

Share, P.-E., Guo, H., Thurber, C. H., Zhang, H., & Ben-Zion, Y. (2019). Seismic imaging of the southern California plate boundary around the south-central transverse ranges using double-difference tomography. *Pure and Applied Geophysics*, *176*(3), 1117–1143. https://doi.org/10.1007/s00024-018-2042-3

Share, P.-E., Peacock, J. R., Constable, S., Vernon, F. L., & Wang, S. (2022a). Structural properties of the southern San Andreas fault zone in northern Coachella Valley from magnetotelluric imaging. *Geophysical Journal International*, *232*(1), 694–704. https://doi.org/10.1093/gji/ggac356

Share, P.-E., Qiu, H., Vernon, F. L., Allam, A. A., Fialko, Y., & Ben-Zion, Y. (2022b). General seismic architecture of the southern San Andreas Fault zone around the Thousand Palms Oasis from a large-N nodal array. *The Seismic Record*, *2*(1), 50–58. https://doi.org/10.1785/0320210040

Shaw, J. H., Plesch, A., Tape, C., Suess, M. P., Jordan, T. H., Ely, G., et al. (2015). Unified structural representation of the southern California crust and upper mantle. *Earth and Planetary Science Letters*, *415*, 1–15. https://doi.org/10.1016/j.epsl.2015.01.016

Shen, Z.-K., King, R. W., Agnew, D. C., Wang, M., Herring, T. A., Dong, D., & Fang, P. (2011). A unified analysis of crustal motion in southern California, 1970–2004: The SCEC crustal motion map. *Journal of Geophysical Research*, *116*(B11), B11402. https://doi.org/10.1029/2011jb008549

Sieh, K., & Williams, P. (1990). Behavior of the southernmost San Andreas fault during the past 300 years. *Journal of Geophysical Research*, *95*(B5), 6629–6645. https://doi.org/10.1029/jb095ib05p06629

Sokal, A. (1997). Monte Carlo methods in statistical mechanics: Foundations and new algorithms. In C. DeWitt-Morette, P. Cartier, & A. Folacci (Eds.), *Functional integration* (Vol. 361, pp. 131–192). Springer US.

SOPAC. (2022). Global navigation satellite system position solutions [Dataset]. Scripps Orbit and Permanent Array Center. Retrieved from http://sopac-csrc.ucsd.edu/index.php/data-download/

Stirling, M. W., Wesnousky, S. G., & Shimazaki, K. (1996). Fault trace complexity, cumulative slip, and the shape of the magnitude-frequency distribution for strike-slip faults: A global survey. *Geophysical Journal International*, *124*(3), 833–868. https://doi.org/10.1111/j.1365-246x.1996.tb05641.x

Thakur, P., Huang, Y., & Kaneko, Y. (2020). Effects of low-velocity fault damage zones on long-term earthquake behaviors on mature strike-slip faults. *Journal of Geophysical Research: Solid Earth*, *125*(8), e2020JB019587. https://doi.org/10.1029/2020jb019587

Tong, X., Sandwell, D., & Fialko, Y. (2010). Coseismic slip model of the 2008 Wenchuan earthquake derived from joint inversion of interferometric synthetic aperture radar, GPS, and field data. *Journal of Geophysical Research*, *115*(B4), B04314. https://doi.org/10.1029/2009jb006625

Tong, X., Sandwell, D. T., & Smith-Konter, B. (2013). High-resolution interseismic velocity data along the San Andreas fault from GPS and InSAR. *Journal of Geophysical Research*, *118*(1), 369–389. https://doi.org/10.1029/2012jb009442

Torres, R., Snoeij, P., Geudtner, D., Bibby, D., Davidson, M., Attema, E., et al. (2012). GMES sentinel-1 mission. *Remote Sensing of Environment*, *120*, 9–24. https://doi.org/10.1016/j.rse.2011.05.028

Tymofyeyeva, E., & Fialko, Y. (2015). Mitigation of atmospheric phase delays in InSAR data, with application to the eastern California shear zone. *Journal of Geophysical Research*, *120*(8), 5952–5963. https://doi.org/10.1002/2015jb011886

Tymofyeyeva, E., & Fialko, Y. (2018). Geodetic evidence for a blind fault segment at the southern end of the San Jacinto fault zone. *Journal of Geophysical Research*, *123*(1), 878–891. https://doi.org/10.1002/2017jb014477

Tymofyeyeva, E., Fialko, Y., Jiang, J., Xu, X., Sandwell, D., Bilham, R., et al. (2019). Slow slip event on the southern San Andreas fault triggered by the 2017 M_w 8.2 Chiapas (Mexico) earthquake. *Journal of Geophysical Research*, *124*(9), 9956–9975. https://doi.org/10.1029/2018jb016765

USGS. (2020). *Quaternary fault and fold database for the nation*. United States Geological Survey. Retrieved from https://www.usgs.gov/programs/earthquake-hazards/faults

Van Der Woerd, J., Klinger, Y., Sieh, K., Tapponnier, P., Ryerson, F. J., & Mériaux, A.-S. (2006). Long-term slip rate of the southern San Andreas fault from [10]Be-[26]Al surface exposure dating of an offset alluvial fan. *Journal of Geophysical Research*, *111*(B4), B04407. https://doi.org/10.1029/2004jb003559

Vavra, E., & Fialko, Y. (2023). Geodetic datasets for analysis of southern San Andreas fault geometry from 2017-2021 shallow creep [Dataset]. Zenodo. https://doi.org/10.5281/zenodo.7719223

Vernon, F., Share, P.-E., Ben-Zion, F. Y., Yehud, & Allam, A. (2020). Southern San Andreas fault zone [Dataset]. International Federation of Digital Seismograph Networks. https://doi.org/10.7914/SN/YA_2020

Wang, K., Xu, X., & Fialko, Y. (2017). Improving burst alignment in TOPS interferometry with Bivariate enhanced spectral diversity (BESD). *IEEE Geoscience and Remote Sensing Letters*, *14*(12), 2423–2427. https://doi.org/10.1109/lgrs.2017.2767575

Yilmaz, z. (2001). *Seismic data analysis*. Society of Exploration Geophysicists.

Zheng, Y., Fattahi, H., Agram, P., Simons, M., & Rosen, P. (2022). On closure phase and systematic bias in multilooked SAR interferometry. *IEEE Transactions on Geoscience and Remote Sensing*, *60*, 1–11. https://doi.org/10.1109/tgrs.2022.3167648

Zigone, D., Ben-Zion, Y., Campillo, M., & Roux, P. (2015). Seismic tomography of the southern California plate boundary region from noise-based Rayleigh and Love waves. *Pure and Applied Geophysics*, *172*(5), 1007–1032. https://doi.org/10.1007/s00024-014-0872-1